

Contents lists available at ScienceDirect

Petroleum Science

journal homepage: www.keaipublishing.com/en/journals/petroleum-science



Original Paper

The geochemical, pore development and water-bearing characteristics of deep and ultra-deep marine shales and their effects on gas content: New implications from the shales of the first Lower Cambrian highyield gas well (Z201) in China



Hai-Tao Gao ^a, Peng Cheng ^{a, *}, Wei Wu ^b, Chao Luo ^b, Liang Xu ^b, Teng-Fei Li ^a, Hai-Feng Gai ^a, Hui Tian ^a

- ^a State Key Laboratory of Deep Earth Processes and Resources, Guangzhou Institute of Geochemisrty, Chinese Academy of Sciences, Guangzhou, 510640, Guangdong, China
- ^b Shale Gas Research Institute, PetroChina Southwest Oil and Gas Field Company, Chengdu, 610051, Sichuan, China

ARTICLE INFO

Article history: Received 28 May 2024 Received in revised form 7 August 2024 Accepted 18 February 2025 Available online 19 February 2025

Edited by Jie Hao and Meng-Jiao Zhou

Keywords: The Lower Cambrian Deep and ultra-deep shales Pore structures Water-bearing characteristics Geochemical characteristics Gas content

ABSTRACT

The Lower Cambrian shales in the Sichuan Basin are considered one of the most promising shale gas resources in China. However, large-scale commercial development has not been achieved due to the relatively low and significantly variable gas contents of the drilled shales. Excitingly, the first major breakthrough in deep and ultra-deep Lower Cambrian shale gas was made recently in the well Z201 in the southern Sichuan Basin, with a gas yield exceeding $73 \times 10^4 \, \mathrm{m}^3 / \mathrm{d}$. The success of well Z201 provides a favorable geological case to reveal the distinct enrichment mechanism of deep and ultra-deep Lower Cambrian shale gas. In this study, at drilling site of well Z201, fresh shale core samples with different gasin-place contents were collected, and their geochemical, pore development and water-bearing characteristics were analyzed systematically. The results showed that the Z201 organic-rich shales reached an overmature stage, with an average Raman maturity of 3.70%. The Z201 shales with high gas-in-place contents are mainly located in the Qiongzhusi 12 section and the upper Qiongzhusi 11 section, with an average gas-in-place content of 10.08 cm³/g. Compared to the shales with low gas-in-place contents, the shales with high gas-in-place contents exhibit higher total organic carbon contents, greater porosities, and lower water saturations, providing more effective pore spaces for shale gas enrichment. The effective pore structures of the deep and ultra-deep Lower Cambrian shales are the primary factors affecting their gas-in-place contents. Similar to the shales with high gas-in-place contents of well Z201, the deep and ultra-deep Lower Cambrian shales in the Mianyang-Changning intracratonic sag, especially in the Ziyang area, generally developed in deep-water shelf facies with high total organic carbon contents and thick sedimentary thickness, providing favorable conditions for the development and preservation of effective pores. Therefore, they are the most promising targets for Lower Cambrian shale gas exploration. © 2025 The Authors. Publishing services by Elsevier B.V. on behalf of KeAi Communications Co. Ltd. This

is an open access article under the CC BY-NC-ND license (http://creativecommons.org/licenses/by-nc-nd/

4.0/).

1. Introduction

In the past two decades, shale gas has emerged as a significant contributor to the increase in natural gas reserves and production (Hao et al., 2013; Jarvie et al., 2007; Jia et al., 2012). With increasing exploration extent, the exploration of shale gas has gradually

* Corresponding author. E-mail address: chengp@gig.ac.cn (P. Cheng). expanded to deep (3500–4500 m) and ultra-deep (>4500 m) layers (Nie et al., 2023; Sun et al., 2021). It is difficult to obtain precise seismic data and typical shale samples from deep and ultra-deep strata, which is a significant challenge in evaluating gas-bearing characteristics and predicting sweet spots in deep and ultra-deep shales (Lei et al., 2021; Zou et al., 2014). The lower Paleozoic marine shales, developed in the Sichuan Basin, have been the focus of shale gas exploration in China, and the deep and ultra-deep shale gas constitutes more than 80% of the shale gas resources, exhibiting enormous resource potential (Li et al., 2021c; Zhou and Zhang,

2023). In recent years, deep and ultra-deep shale gas has become the main exploration goal in the southern Sichuan Basin, and the first 10¹² m³ shale gas field of the deep Longmaxi Formation in China was built in the Luzhou block (Borjigin et al., 2017; Li et al., 2024; Wu et al., 2023). Despite significant advancements in deep and ultra-deep shale gas exploration in the Sichuan Basin, the overall exploration extents and performances have not met expectations. Although the Lower Cambrian and Upper Ordovician-Lower Silurian organic-rich shales developed in the Sichuan Basin, but more than 90% of commercial shale gas was produced from the latter shales (Feng et al., 2023a; Zou et al., 2019). The Lower Cambrian shales developed in the Sichuan Basin are characterized by large thicknesses, stable distributions, and higher total organic carbon (TOC) contents, making them important scopes for the exploration of shale gas (Dai et al., 2021; Yan et al., 2016). Compared to the Lower Silurian shales, the Lower Cambrian shales developed at earlier ages, buried at greater depths, and reached greater maturity stages (Li et al., 2022a; Xiao et al., 2015). In addition, the sedimentary environments of the Lower Cambrian shales exhibit significant differences in various regions and formations, and exhibit significant differences in gas-in-place (GIP) contents (Zhang et al., 2018).

As an unconventional natural gas resource, shale gas is characterized by self-generation and storage. The generation and accumulation of shale gas are closely related to the water-bearing, pore development, and geochemical characteristics of shales (Ross and Bustin, 2009). The gas generation potential and development of OM pores are controlled by the content, type and maturity of organic matter (OM) in shales (Gai et al., 2018; Zhang et al., 2012). Moreover, the composition and content of clay minerals in shales influence the development and preservation of inorganic matter (IM) pores. Shale strata commonly contain complex pore systems with different pore widths and types, among which, the distribution and occurrence of shale gas vary (Feng et al., 2023b; Loucks et al., 2009). Therefore, the development characteristics of shale pores are critical for their GIP contents (Curtis, 2002; Loucks et al., 2012). Moreover, shale strata generally contain water in pore systems, which competes with shale gas, and the distribution and occurrence of pore water largely influence the GIP contents of shales (Cheng et al., 2022; Ukaomah et al., 2023).

The geological, geochemical, mineral composition, and pore structure distributions (PSDs) of the shallow Lower Cambrian shales in the Sichuan Basin and surrounding areas have been well documented in previous studies, and these characteristics exhibit significant differences in different regions and formations (Zhang et al., 2019). The Lower Cambrian shales in northern Guizhou and western Hubei have evolved to highly mature or overmature stages, with equivalent vitrinite reflectivity (EqV R_0) of 2.8%–4.0%. The shales have TOC contents between 2.8% and 4.0% (Li et al., 2017; Tian et al., 2015). For the Lower Cambrian shales in northern Guizhou, the feldspar, clay and carbonate mineral contents are 54%, 33%, and 7%, respectively, while they are 33%, 35%, and 27%, respectively, for the Lower Cambrian shale in western Hubei (Han et al., 2013; Wang et al., 2016). Additionally, the pore development degree in Lower Cambrian shales is generally less than that in Lower Silurian shales and differs in various regions and formations. For example, in northern Guizhou, the Lower Cambrian shales are generally composed of OM pores with pore widths <30 nm (Wang et al., 2016), while those in western Hubei are largely composed of OM pores and dissolution IM pores with pore widths <50 nm (Dong et al., 2024; Miao et al., 2023).

In the Sichuan Basin and surrounding areas, the Lower Cambrian shales are widely distributed, and their thicknesses, burial depths, and depositional environments exhibit significant differences in various regions (Chen et al., 2017; Zhang et al., 2020). Within the

Mianyang-Changning intracratonic sag, the Lower Cambrian shales were developed in deep-water shelf facies and have the greatest burial depth and thickness, which implies a large shale gas potential (Wang et al., 2021; Wu et al., 2019). However, because of the lack of typical deep and ultra-deep shale samples, the geological characteristics of these shales are poorly understood.

Compared with the Lower Silurian shales, the Lower Cambrian shales have a lower GIP content and obviously vary in different regions and formations. Several explorations have been proposed for this issue in previous studies. The prevailing view is that the Lower Cambrian shale underwent significant hydrocarbon expulsion at the oil generation stage, and the residual hydrocarbons were limited, which reduced the generation of shale gas in high maturity stage (Liu et al., 2020). Some studies suggest that this is mainly because the types of OM in the Lower Cambrian shales differ from those in the Lower Silurian shales and significantly vary with changes in depositional environment (Tan et al., 2015). In addition, complex multistage tectonic transformations may be the main factors influencing the GIP content of the Lower Silurian shales (Huo et al., 2022; Liu et al., 2018). At present, however, little is known about the gas-bearing properties of the deep and ultra-deep Lower Cambrian shales, which is still a challenge in shale gas exploration.

Recently, in the southern Sichuan Basin, the Lower Cambrian shale gas exploration made the first major breakthrough in the deep and ultra-deep Qiongzhusi shales of well Z201, with daily production exceeding 73×10^4 m³. The exciting breakthrough of well Z201 greatly enhanced the confidence of shale gas exploration in the deep and ultra-deep Lower Cambrian shales and provided a favorable geological case for revealing its unique enrichment mechanism. In this study, the deep and ultra-deep Lower Cambrian fresh core shale samples at different intervals were collected from the well Z201 drilling site. To reveal the main reason for the high GIP content, the reservoir characteristics of the Z201 shales, including water-bearing, pore development, and geochemical characteristics, were analyzed systematically. The results can enhance the understanding of ultra-deep shale gas accumulation and offer new insights for the exploration and development of the Lower Cambrian shale gas, which may have significant theoretical and practical implications.

2. Geological background

The Sichuan Basin is a large superimposed basin located on the western margin of the Yangtze Plate, and it is a secondary tectonic unit of the Yangtze Craton (Wang et al., 2016; Jiang et al., 2023). During the Later Cambrian-Early Ordovician, due to the Tongwan and Xingkai movements, the structural stress in the Sichuan Basin changed from compressive to extensional and resulted in the formation of the Mianyang-Changning intracratonic sag (Liu et al., 2018; Liu et al., 2012). The Lower Cambrian Qiongzhusi shales are widely distributed in the Sichuan Basin, with whose thickness and distribution are mainly controlled by the intracratonic sag (Li et al., 2022b; Wei et al., 2020). In the intracratonic sag, the Qiongzhusi shale developed in deep-water shelf facies, and its thickness gradually decreased from exceeding 400 m in the center of the intracratonic sag to less than 100 m in the margin areas (Fig. 1(a)). According to lithological characteristics, the Qiongzhusi Formation can be divided into two sections. The lower section is mainly composed of black, gray-black, and light gray mudstone and silty mudstone, with thin layers of siliceous rocks and carbonate rocks developed locally. The upper section is mainly composed of dark gray, gray, and gray-green argillaceous siltstone and siltstone, with thin layers of fine sandstone and carbonate rocks (Fig. 1(b)).

3. Samples and experiments

3.1. Samples

In this study, a total of 14 Lower Cambrian Oiongzhusi shale samples were collected from well Z201, including 10 ultra-deep shale samples from the Oiongzhusi 1 member (O1) section, with burial depths between 4500 m and 4900 m, and 4 deep shale samples from the Qiongzhusi 2 member (Q2) section, with burial depths between 4400 m and 4500 m. At the drilling site of well Z201, after the shale core was brought to the surface, the mud on the surface of the core was wiped off using absorbent paper. The shale core in the target interval was crushed into large pieces and submerged in water, and the bubble release degree was used to preliminarily determine the extent of gas bearing in the shale. Shale samples from gas-bearing intervals were selected, and small shale plungers (2.5 cm \times 2.0 cm) were drilled from the inside of the fresh shale cores. The drilled shale plunger samples were immediately sealed in ziplock bags, placed in a low-temperature box, and analyzed in the laboratory. The gas in the shales can prevents the entry of external water, and the as-received shale plungers serve as proximate representations of the water-bearing characteristics of the shales under geological conditions (Cheng et al., 2018).

3.2. Experiments

3.2.1. TOC contents and mineral compositions

A portion of the shale plunger sample was crushed to a size <80 mesh (0.2 mm), and the shale particle sample was placed into a crucible after weighing. A 5% dilute hydrochloric acid solution was added to the crucible, and heated at $80\,^{\circ}\text{C}$ for 4 h to dissolution carbonate minerals in shale samples. Next, the shale sample was washed several times with deionized water to remove residual chloride ions, dried at $105\,^{\circ}\text{C}$ for $12\,\text{h}$ and weighed again. Subsequently, the TOC content of the shale sample was analyzed by a Leco CS-230 carbon-sulfur analyzer.

A portion of the shale plunger sample was crushed to a size <200 mesh (<0.074 mm), and dried at 120 °C for 10 h. Then, a Bruker D8 Advance X-ray diffractometer (XRD) was used to analyze the mineral composition of the shale sample. The instrument operate with a voltage and current of 40 kV and 30 mA, respectively, and the XRD pattern was measured with a scanned step size of 0.02° (2θ) and a range of 3°–85°. The peak area integration method was used to calculate the relative mineral content of the shale sample (Chalmers and Bustin, 2008). Based on the mineral compositions, the brittleness index of the shale was calculated by Eq. (1) (Chen and Xiao, 2013; Rybacki et al., 2016).

OM was characterized using the ratio of the height of the D peak (Dh) and G peak (Gh) (Liu et al., 2013), and the $_{Rmc}R_0\%$ was calculated by Eq. (2):

$$_{\rm Rmc}R_{\rm o}\% = 1.1659h \left(\frac{{\rm Dh}}{{\rm Gh}}\right) + 2.7588$$
 (2)

where h(Dh/Gh) represents the ratio of the height of the D peak (Dh) to that of the G peak (Gh).

3.2.3. Porosity and pore structure

The shale porosity (Φ) was calculated using the bulk density (ρ_{bulk}) and skeleton density (ρ_{skeletal}) (Yu et al., 2018). The ρ_{skeletal} of the dried shales was measured using a Quantachrome Ultrapyc 1200e helium density meter. After first weighing (m_1 , g), the shale block was sealed with wax and weighed again (m_2 , g). The mass of the sealed shale block was measured (m_3 , g) using a DAHO-120 M high-precision electronic hydrometer. Then, the ρ_{bulk} and porosity of the shale are calculated by Eqs. (3) and (4), respectively.

$$\rho_{\text{bulk}} = m_1 / (m_2 - m_3 - (m_2 - m_1) / \rho_c) \tag{3}$$

$$\Phi = 100\% \times (1 - \rho_{\text{bulk}} / \rho_{\text{skeletal}}) \tag{4}$$

where ρ_c is the density of the wax, which is 0.9136 g/cm³, and the density of the deionized water is 1 g/cm³.

The non-micropore (>2 nm) and micropore (<2 nm) of the shales were measured by low-pressure N_2 adsorption (LPNA) and CO_2 (LPCA) experiments, respectively. The measurements were conducted using a Micromeritics ASAP 2020 M adsorption instrument. First, the as-received shale sample was crushed to 20-40 mesh (0.45 mm-0.84 mm) and divided into two parts: one part was dried, and the other part was kept under as-received condition. The LPNA measurement was performed at a relative pressure (P/P_0) of 0.005-0.995 at -196 °C (liquid nitrogen). The Barrett–Joyner–Halenda (BJH) model and Brunauer–Emmett–Teller (BET) model were used to calculate the pore volume (PV) and specific surface area (SSA) of non-micropores, respectively. The LPCA measurements were set with a P/P_0 of 0.00001-0.032 at 0 °C (ice–water mixture), and the PV and SSA of the micropores were calculated by the density functional theory (DFT) model.

3.2.4. Scanning electron microscope (SEM)

The as-received shale sample was cut into small pieces of 1.0 cm \times 1.0 cm \times 0.4 cm perpendicular to bedding plane. Firstly, the surface of the sample was mechanically polished, followed by argon ion polishing for 4 h. Finally, the micro pore structure of the sample was observed using Hitachi S8010 field emission scanning electron

$$Brittleness\ Index = \frac{(Dolomite + Calcite + Feldspar + Quartz) \times 100\%}{Clay + Dolomite + Calcite + Feldspar + Quartz}$$

$$(1)$$

3.2.2. Thermal maturity measurement

A shale block sample was used to prepare polished sections. A HORIBA-JY LabRAM fully automatic microscopic Raman spectrometer was used to measure the Raman spectra of the OM in the shale. A $50\times$ objective lens and a He-Ne laser with an intensity set at 30 mV and a wavelength of 532 nm were used in the measurement. The exposure time and scanning range were $10 \text{ s}{-}20 \text{ s}$ and $500 \text{ cm}^{-1}{-}3000 \text{ cm}^{-1}$, respectively. At least 5 OM particles were measured for each shale sample. The Raman reflectivity (${}_{\text{Rmc}}R_0\%$) of

microscopy (FE-SEM). During the experiment, the working distance of the SEM was set at 1.5 mm-4.0 mm, and the acceleration voltage was 1 kV-3 kV.

3.2.5. Pore water content (C_{PW}) and water saturation (S_W)

The as-received shale sample was weighed to obtain the initial mass (m_{AR} , g), after which the sample was dried at 120 °C for 12 h and weighed multiple times until the mass remained basically consistent (with a maximum error of no more than 3% for three

consecutive measurements) to obtain the mass of the dried shale sample ($m_{\rm Dry}$, g). The $C_{\rm PW}$ and $S_{\rm W}$ were calculated by Eqs. (5) and (6), respectively (Cheng et al., 2018):

$$C_{PW} = (m_{AR} - m_{Dry}) \times 1000 / m_{Dry}$$
 (5)

$$S_{W} = C_{PW} \times \rho_{bulk} / (10 \times \Phi \times \rho_{w})$$
 (6)

where $\rho_{\rm w}$ is the density of water and was taken as 1 g/cm³.

4. Results and discussion

4.1. GIP contents of the Z201 shales

The GIP content varies in different Qiongzhusi shale strata. The shales with high GIP content ($S_{\rm HG}$) are mainly located in the upper Q1₁ section and the Q1₂ section, with burial depths of 4557.6–4852.0 m. The GIP contents of the $S_{\rm HG}$ were in the range of 6.06–14.25 cm³/g, with an average value of 10.08 cm³/g (Table 1 and Fig. 2). The shales with low GIP content ($S_{\rm LG}$) are located in the Q2 section and the lower Q1₁ section, with burial depths of 4469.1–4486.1 m and 4858.9–4879.9 m, respectively. The GIP contents of the $S_{\rm LG}$ were in the range of 3.25–5.37 cm³/g, with an average value of 4.54 cm³/g (Table 1 and Fig. 2). Overall, the GIP content of the Z201 shales initially increases and then decreases with the increasing of burial depth, and the sweet spots of shale gas are the Q1₂ section and the upper Q1₁ section (Table 1 and Fig. 2).

4.2. TOC content, maturity, and mineral composition of the Z201 shales

OM is abundant in the Z201 shales, with TOC contents in the range of 1.43%-6.90%, with an average of 3.40% (Table 1). As the burial depth increases, the TOC contents first increase and then decrease. For the S_{LG} , the TOC contents are in the range of 1.53%-4.12%, with an average of 2.25%, and those of the S_{HG} are in the range of 1.70%-6.90%, with an average of 4.26%. The TOC content of the former shales is much lower than that of the latter shales (Table 1). OM in the Z201 shales has evolved to overmature stages, with $R_{Rmc}R_0$ are in the range of 3.68%-3.73%, with an average of 3.70% (Table 1 and Fig. 3). The maturity of the OM in the Z201 shales is basically greater than that in the Lower Silurian shales (Cheng et al., 2018).

The Z201 shales are mainly composed of quartz, feldspar and clay minerals. The contents of quartz are in the range of 16.8%—78.0%, with an average of 29.23%. The contents of feldspar are in the

range of 2.3%-39.8%, with an average of 21.41%. The contents of clay minerals are in the range of 11.2%-62.5%, with an average of 42.5%. Additionally, the Z201 shales contain small amounts of minerals such as calcite, dolomite, and pyrite, whose contents are generally less than 5.0% (Table 1). Compared to the Longmaxi shales, the Z201 shales have lower quartz and clay mineral contents but significantly higher feldspar contents (Li et al., 2018). The average contents of quartz, feldspar and clay minerals in S_{LG} are 38.4%, 14.2% and 41.3%, respectively, but in S_{HG} , they are 22.4%, 26.8%, and 43.4%, respectively. The brittleness index of the shales are in the range of 36.93%-88.63%, with an average of 56.88% (Table 1). The brittleness index of S_{LG} are in the range of 41.50%-87.92%, with an average of 58.23%, and those of S_{HG} are 42.70%-63.39%, with an average of 55.86%. The brittleness index of the former shales is basically consistent with the latter shales.

4.3. Pore characteristics and influencing factors

4.3.1. Porosity and pore structure

The porosities of the deep and ultra-deep Z201 shales are in the range of 1.87%-6.16%, with an average of 4.46%. The average porosities of S_{LG} and S_{HG} are 3.20% and 5.41%, respectively, and the average porosity of the former shales is much lower than that of the latter shales (Table 1 and Fig. 4). The Z201 shales developed abundant nanopores (Table 2). The average SSA of micropores, nonmicropores, and total pores are 15.29, 16.81, and 32.10 m^2/g , respectively. The average PV of micropores, non-micropores, and total pores are 0.0024, 0.0161, and 0.0185 cm³/g, respectively (Table 2). The average SSA of the micropores, non-micropores, and total pores are 13.26, 12.63, and 25.89 m²/g, respectively, for S_{LG} and 16.81, 19.94, and 36.75 m^2/g , respectively, for S_{HG} (Table 2). The average PV of the micropores, non-micropores, and total pores were 0.0021, 0.0145, and 0.0165 cm³/g, respectively, for the S_{LG} and 0.0027, 0.0174, and 0.0200 cm 3 /g, respectively, for the S_{HG} (Table 2). The pore structures of S_{LG} are significantly smaller than those of S_{HG} .

4.3.2. Influencing factors of pore development

The compositions and contents of OM and IM in shales have a decisive influence on pore development characteristics. For the $S_{\rm LG}$, the TOC content and brittleness index exhibited strong positive correlations with the SSA and PV of micropores and negative correlations with the SSA and PV of non-micropores. In addition, the clay minerals content shows negative correlations with the SSA and PV of micropores and a positive correlation with the PV of non-micropores (Fig. 4(a)–(f)). For the $S_{\rm HG}$, the TOC content shows

Table 1Geological, geochemical, water-bearing, porosity, and GIP characteristics of the deep and ultra-deep Z201 shales.

Samples	Depth, m	Formation	TOC, %	_{Rmc} R _o , %	Minerals content, %				BI, %	Ф, %	C _{pw} , mg/g	S _w , %	GIP, cm ³ /g	Туре		
					Quartz	Feldspar	Calcite	Dolomite	Pyrite	Clay						
Z201-18	4469.1	Q2	1.70		18.5	18.4	2.2	1.9	1.2	57.8	41.50	4.20	8.87	38.57	3.25	S_{LG}
Z201-25	4476.2	Q2	1.43		19.5	15.4	4.5	3.7	1.4	55.5	43.71	2.71	10.43	35.04	4.74	
Z201-29	4480.0	Q2	1.93	3.68	16.8	12.7	4.5	2.6	0.9	62.5	36.93	3.98	9.41	31.25	4.55	
Z201-35	4486.1	Q2	1.53		20.0	28.9	1.4	2.2	1.5	46.0	53.30	4.07	7.32	23.72	5.12	
Z201-85	4577.6	Q1 ₂	1.70	3.70	19.4	20.3	1.4	1.0	1.4	56.5	42.70	6.16	7.85	29.85	6.06	$S_{\rm HG}$
Z201-102	4594.5	$Q1_2$	3.28		18.8	31.1	0.6	0.7	1.3	47.5	51.87	6.05	8.23	19.53	7.56	
Z201-108	4600.4	$Q1_2$	4.53		17.5	39.8	1.9	0.8	1.5	38.5	60.91	6.12	9.24	17.41	11.46	
Z201-112	4604.5	$Q1_2$	5.82		18.6	34.7	2.4	1.0	2.3	41.0	58.03	4.95	11.19	17.83	8.73	
Z201-154	4762.5	Q1 ₁	1.76		18.0	15.0	5.5	16.8	1.8	42.9	56.31	4.08	6.25	23.59	8.78	
Z201-177	4786.1	Q1 ₁	4.35		28.0	23.7	3.3	1.1	1.3	42.6	56.84	5.41	8.76	28.32	10.91	
Z201-186	4795.5	Q1 ₁	5.73		25.0	24.6	2.2	4.2	1.5	42.5	56.85	5.89	8.98	21.26	14.25	
Z201-203	4852.0	Q1 ₁	6.90	3.73	33.8	25.5	1.8	0.9	2.2	35.8	63.39	4.60	9.39	27.54	12.89	
Z201-210	4858.9	Q1 ₁	2.78	3.68	77.3	2.3	4.1	3.6	1.5	11.2	88.63	2.36	2.47	22.06	5.37	S_{LG}
Z201-212	4879.9	Q1 ₁	4.12		78.0	7.3	0.0	0.0	0.0	14.7	85.30	1.87	6.83	8.24	4.20	

Note: BI—brittleness index; Φ —porosity; C_{pw} —pore water content; S_{w} —water saturation; GIP—gas-in-place.

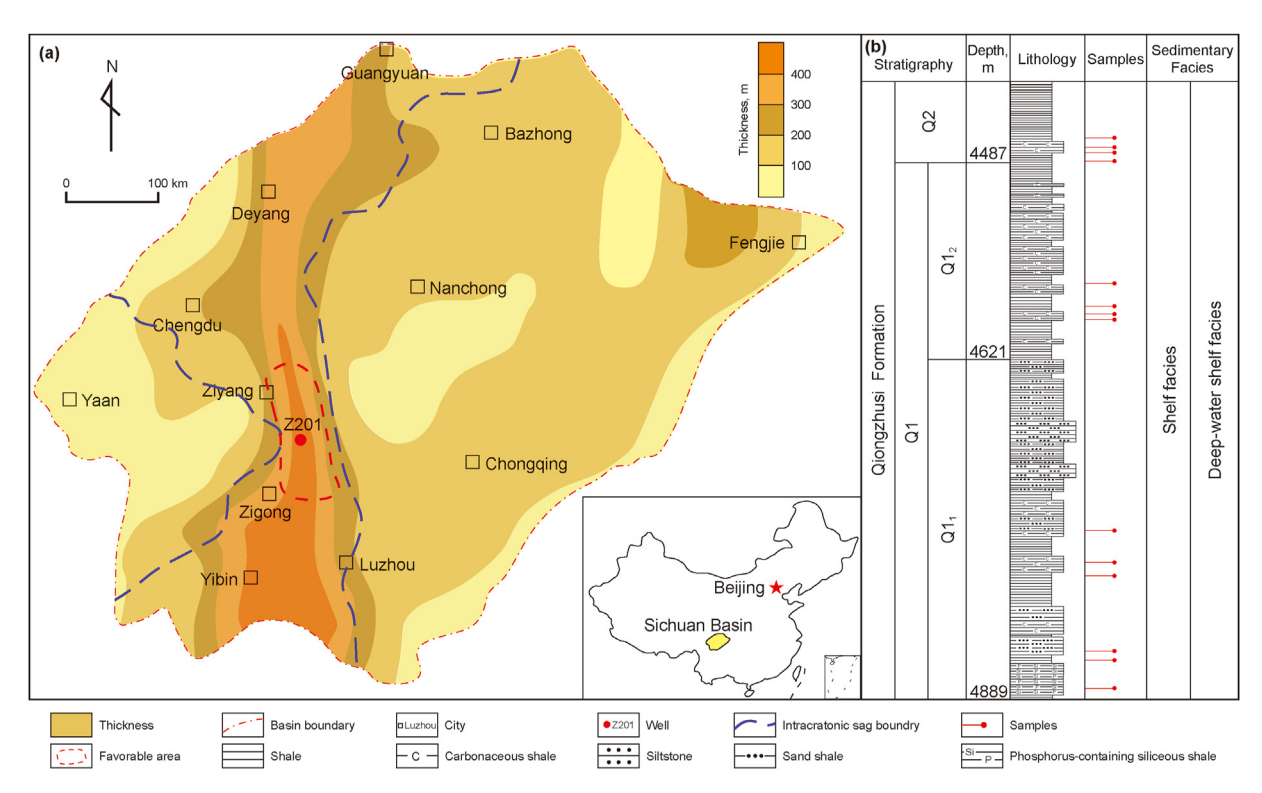
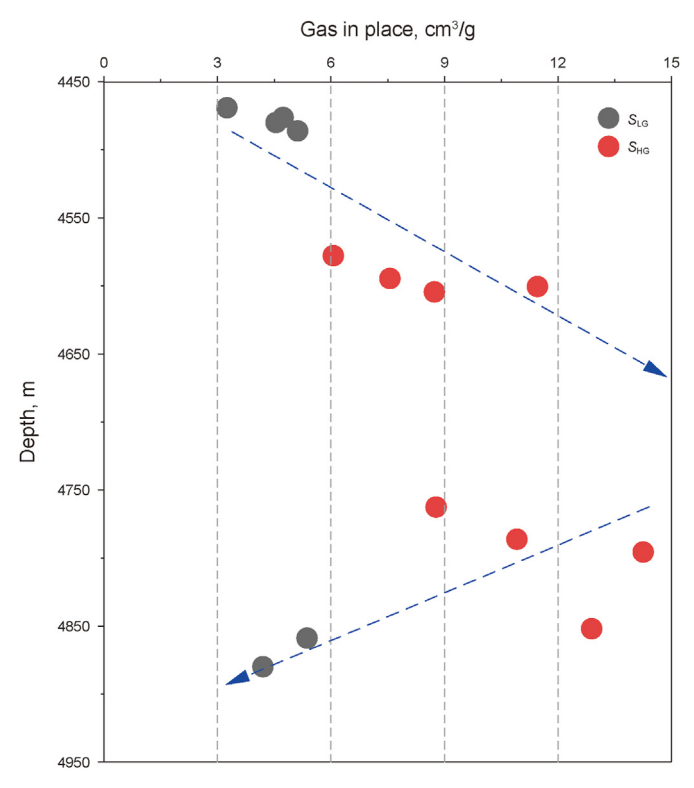


Fig. 1. Sketch map showing the thickness of the Lower Cambrian strata in the Sichuan Basin (a) and the location and stratigraphic column of well Z201 (b) (modified from Jiang et al. (2023)).



 $\begin{tabular}{ll} \textbf{Fig. 2.} & \textbf{Differences} & \textbf{in the gas-in-place (GIP) contents of the deep and ultra-deep Z201 shales. \end{tabular}$

strong positive correlations with the SSA and PV of micropores and weak positive correlations with the SSA and PV of non-micropores. However, there are no apparent linear correlations between the brittleness index and clay minerals with pore structures (Fig. 4(g)-(i)).

There are significant differences in pore types and structures between S_{LG} and S_{HG} . According to the correlations between the shale composition and pore structures (Fig. 4), the S_{LG} micropores mainly consist of OM pores and a small amount of brittle mineral-hosted pores. The linear regression analysis results indicate that OM pores contribute more than 54% and 85% to the SSA and PV of micropores, respectively, while non-micropores are mainly clay-hosted pores (Fig. 5(a), (b)). Both the micropores and non-micropores of S_{HG} are primarily OM pores. OM pores contribute more than 53% and 70% to the SSA and PV of micropores, respectively. OM pores contribute more than 50% to the SSA of non-micropores. IM pores, including brittle mineral-hosted and clay-hosted pores, barely developed in the S_{HG} (Fig. 5(c), (d)).

Compared to the S_{LG} and the Lower Cambrian shales in other areas, the S_{HG} has well-developed OM pores, with a larger SSA and PV. The TOC contents of the S_{HG} are in the range of 1.70%–6.90%, with an average of 4.26%; the $R_{MC}R_0$ reaches 3.70%, indicating a high degree of thermal evolution. The thermal evolution process can form a large number of OM pores, providing substantial space for the occurrence of shale gas (Xie et al., 2023; Yang and Guo, 2020). Additionally, the S_{HG} have a high brittleness index. During the burial process, abundant brittle minerals can form particle frameworks that effectively resist external pressure, providing support and protecting OM pores (Katsube and Williamson, 1994; Zhang et al., 2023).

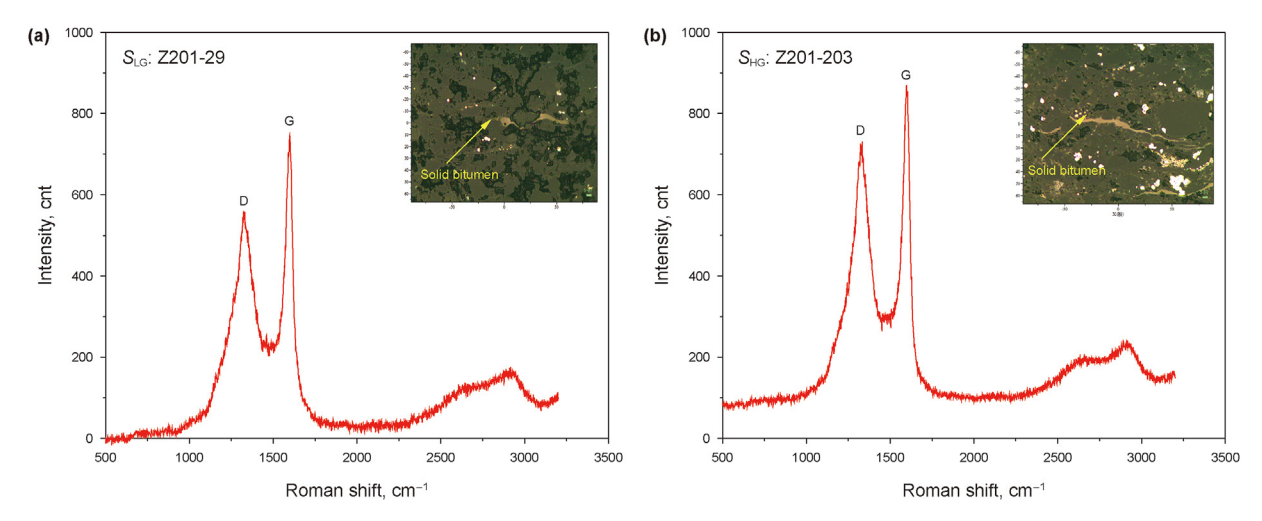


Fig. 3. Raman spectra of the typical deep and ultra-deep Z201 shales.

4.4. Water-bearing characteristics and influencing factors

4.4.1. C_{PW} and S_W

The Z201 shales have a low $C_{\rm PW}$ and $S_{\rm W}$, and the $C_{\rm PW}$ is in the range of 2.47–11.19 mg/g, with an average of 8.23 mg/g; the $S_{\rm W}$ is in the range of 8.24%–38.57%, with an average of 24.59%. The $C_{\rm PW}$ of $S_{\rm LG}$ was in the range of 2.47–10.43 mg/g, with an average of 7.56 mg/g, and that of $S_{\rm HG}$ was in the range of 6.25–11.19 mg/g, with an average of 8.74 mg/g. The $S_{\rm W}$ of $S_{\rm LG}$ was in the range of 8.24%–38.57%, with an average of 26.48%, and that of $S_{\rm HG}$ was in the range of 17.41%–29.85%, with an average of 23.17% (Table 1). The $C_{\rm PW}$ of $S_{\rm LG}$ is smaller than that of $S_{\rm HG}$, and the $S_{\rm W}$ of $S_{\rm LG}$ is much greater than that of $S_{\rm HG}$.

4.4.2. Influencing factors of water-bearing characteristics

The compositions and contents of OM and IM in shales have a decisive influence on the C_{PW} and S_W (Chang et al., 2022). For the S_{LG} , the C_{PW} and S_W exhibited negative correlations with the TOC content and brittleness index and positive correlations with the clay minerals content (Fig. 6). For the S_{HG} , the C_{PW} exhibits positive correlations with the TOC and clay minerals content and a negative correlation with the brittleness index, while the S_W exhibits negative correlations with the TOC content and brittleness index and a positive correlation with the clay minerals content (Fig. 6).

The correlation results suggest that the C_{PW} and S_W are primarily controlled by the clay minerals content; in addition, water can also exist in OM pores. The $_{Rmc}R_o$ of the Z201 shales reaches 3.70%, indicating an overmature degree, which is strongly hydrophobic, and a higher TOC content can lead to a decrease in S_W . However, the oxygen-containing functional groups in OM can bind and adsorb water to OM pores (Cheng and Heidari, 2018; Li et al., 2016). Brittle minerals are hydrophobic and lack oxygen-containing functional groups, which is unfavorable for water adsorption and storage (Cheng and Heidari, 2018; Li et al., 2016). Clay minerals, on the other hand, are hydrophilic (Berend et al., 1995). Clay minerals can develop abundant interlayer pores, which are the main adsorption and storage spaces for pore water (Anderson et al., 2019; Mu et al., 2021).

The occurrence and distribution of water are determined by the pore structure (Cheng et al., 2023). For the S_{LG} , the C_{PW} and S_{W} exhibited negative correlations with the SSA and PV of micropores, the C_{PW} exhibited positive correlations with the SSA and PV of the nonmicropores, and the S_{W} exhibited no linear correlations with the SSA and PV of the nonmicropores. For the S_{HG} , the C_{PW} exhibits

strong positive correlations with the SSA and PV, and the S_W exhibits negative correlations with the SSA and PV (Fig. 7).

The different correlations between pore structures and C_{PW} and S_W of the Z201 shales are mainly related to the pore development characteristics. The micropores in the Z201 shales are primarily composed of OM pores and a small amount of brittle mineral-hosted pores. Both OM and brittle minerals are hydrophobic and unfavorable for water occurrence. The non-micropores of the Z201 shales were mainly provided by OM and clay-hosted pores, and clay minerals exhibit strong hydrophilicity, with clay-hosted pores serving as the primary space for pore water.

4.5. Effective pore structures of the deep and ultra-deep Z201 shales

4.5.1. Influence of water-bearing characteristics on pore structures

Shale strata generally contain water under geological conditions. Pore water can affect the pore structures by occupying or blocking part of the pore space (Lu et al., 2020; Zeng et al., 2019). The effects of pore water on pore structures can be indicated by the differences in the LPCA/LPNA isotherms of the shales under asreceived and dried conditions.

The LPCA isotherm patterns of the Z201 shales under asreceived and dried conditions exhibit similar shapes. With increasing P/P_0 , the quantity of adsorbed CO_2 gradually increases, resulting in a typical Type I adsorption isotherm characterized by micropore filling and monolayer adsorption (Fig. 8(a)) (Lu et al., 2020; Zeng et al., 2019), which indicates a large number of micropores in the Z201 shales. However, the LPNA isotherm patterns of the shales under as-received and dried conditions show significant differences. As P/P_0 increases, the quantity of adsorbed N_2 gradually increases but does not reach adsorption saturation when P/P_0 approaches 1.0, which indicates the presence of a certain amount of mesopores and macropores in shales (Kuila and Prasad, 2013; Tian et al., 2013). In addition, there are obvious hysteresis loops between the adsorption and desorption curves, and the morphology of the hysteresis loops indicates that the pores of the Z201 shales mainly exhibit ink bottle-shaped pores and parallel plate-like narrow slit pores (Fig. 8(b)) (Ghanizadeh et al., 2015). The adsorption capacity and morphology of the hysteresis loops of the as-received shales are much smaller than those of the dried shales, indicating that pore water can change effective pore structures by occupying certain pore spaces of shales (Gao et al., 2023). Under dried and asreceived conditions, the LPCA/LPNA isotherms of S_{LG} are lower than those of S_{HG} , which indicates that the former shales have smaller

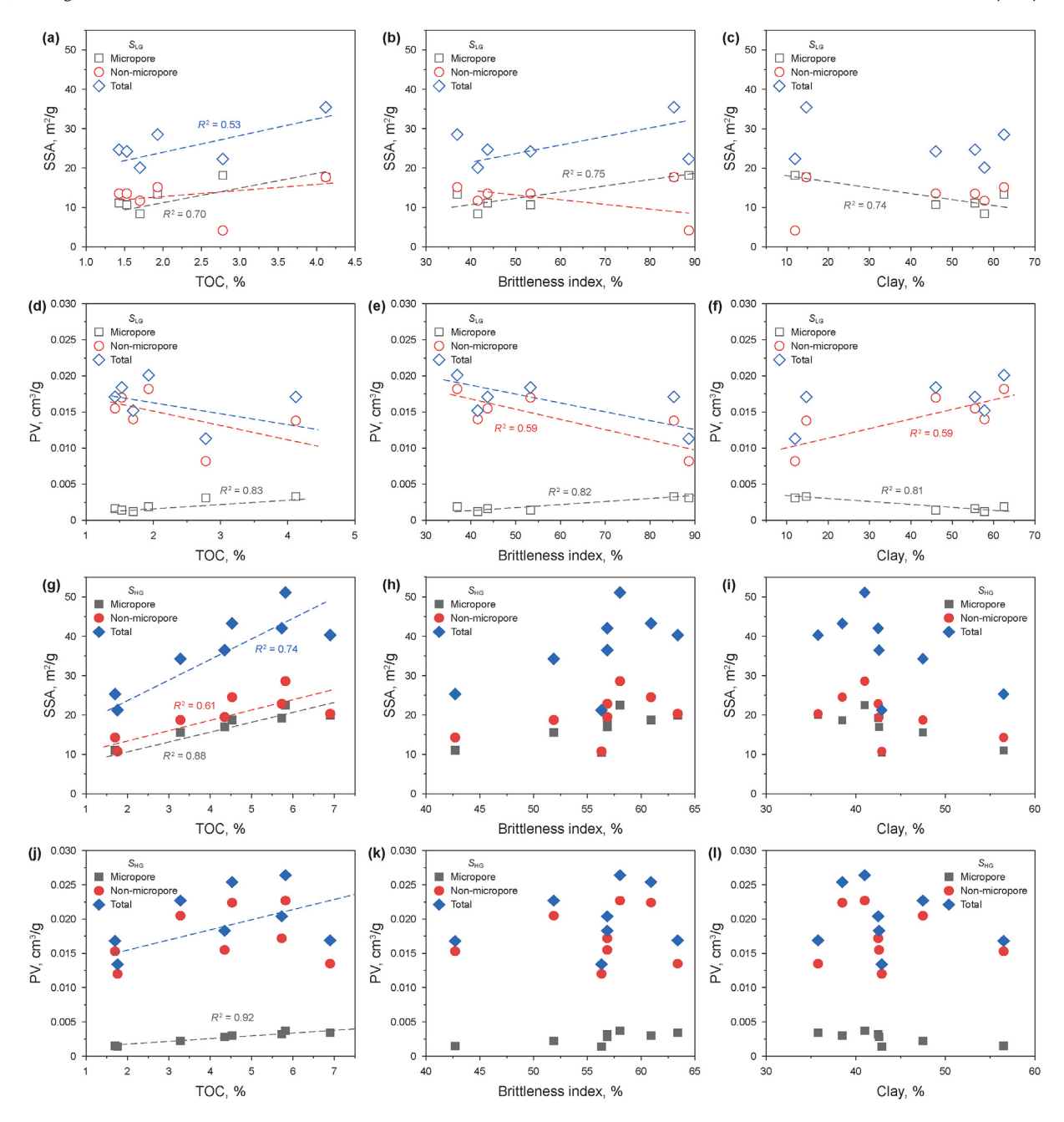


Fig. 4. Correlations between the total organic carbon (TOC) content ((a), (d), (g), (j)), brittleness index ((b), (e), (h), (k)), clay minerals content ((c), (f), (i), (l)) and specific surface area (SSA) and pore volume (PV) of the deep and ultra-deep Z201 shales.

pore structures than the latter shales (Fig. 8).

The PSDs of micropores PV for the Z201 shales are similar under dried and as-received conditions and exhibit a "bimodal" distribution, with peak pore widths of 0.80-0.90 nm and 0.45-0.65 nm, respectively (Fig. 9(a)). Notably, all of the micropore volumes disappeared in the PSDs when the pore widths <0.45 nm, which may be attributed to the fact that the micropores of shales with pore widths <0.45 nm were completely occupied or blocked by water under as-received condition (Fig. 9(a)). The PSDs of non-micropores were smaller for the Z201 shales under as-received condition than for those under dried condition and exhibited different distribution characteristics under different conditions. With the increase of pore

width, the PSDs of non-micropores SSA gradually decrease for the dried shales but exhibit a "unimodal" distribution with a peak at a pore width of 5 nm for the as-received shales. Additionally, the PSDs of the non-micropores PV exhibited a similar unimodal distribution pattern for both the as-received and dried shales, with the peak value also occurring at the pore width of 5 nm (Fig. 9(b), (c)). The PSDs of non-micropores indicate that when the pore width is < 20 nm, the non-micropore structures of the Z201 shales under as-received condition are smaller than those under dried condition, and the difference becomes more pronounced when the pore width is <10 nm. This indicates that in the Z201 shales, pore water is primarily present in pores <20 nm, especially those <10 nm.

Table 2Pore structure characteristics of the deep and ultra-deep Z201 shales under as-received and dried conditions.

Samples	SSA, m ² /g							PV, cm ³ /g						
	As-received			Dried			As-received	d		Dried			_	
	Micropo	res Non- micropores	Total pores	Micropoi	res Non- micropores	Total pores	Micropores	Non- micropores	Total pores	Micropore	s Non- micropores	Total pores	_	
Z201-18	7.23	1.67	8.90	8.41	11.71	20.12	0.0008	0.0076	0.0084	0.0012	0.0140	0.0152	S_{LG}	
Z201-25	9.76	1.59	11.35	11.15	13.53	24.68	0.0011	0.0074	0.0085	0.0016	0.0155	0.0171		
Z201-29	10.32	2.41	12.73	13.35	15.16	28.51	0.0012	0.0103	0.0115	0.0019	0.0182	0.0201		
Z201-35	9.42	3.55	12.97	10.71	13.54	24.25	0.0011	0.0127	0.0138	0.0014	0.0170	0.0184		
Z201-85	9.31	2.04	11.35	11.03	14.30	25.33	0.0011	0.0089	0.0100	0.0015	0.0153	0.0168	S_{HG}	
Z201-102	12.70	5.24	17.94	15.55	18.73	34.28	0.0018	0.0158	0.0176	0.0022	0.0205	0.0227		
Z201-108	16.63	7.38	24.01	18.71	24.54	43.25	0.0025	0.0171	0.0196	0.0030	0.0224	0.0254		
Z201-112	19.60	6.65	26.25	22.50	28.60	51.10	0.0031	0.0140	0.0171	0.0037	0.0227	0.0264		
Z201-154	8.20	2.48	10.68	10.48	10.75	21.23	0.0010	0.0097	0.0107	0.0014	0.0120	0.0134		
Z201-177	15.59	4.05	19.64	17.00	19.47	36.47	0.0024	0.0113	0.0137	0.0028	0.0155	0.0183		
Z201-186	16.20	4.56	20.76	19.19	22.84	42.03	0.0027	0.0115	0.0142	0.0032	0.0172	0.0204		
Z201-203	16.16	1.33	17.49	20.00	20.30	40.30	0.0029	0.0067	0.0096	0.0034	0.0135	0.0169		
Z201-210	3.94	1.89	5.83	18.17	4.16	22.33	0.0010	0.0044	0.0054	0.0031	0.0082	0.0113	S_{LG}	
Z201-212	15.26	2.75	18.01	17.75	17.70	35.45	0.0027	0.0089	0.0116	0.0033	0.0138	0.0171		

Note: SSA—specific surface area; PV—pore volume.

4.5.2. Effective pore structures of the Z201 shales

The various in pore structures of the Z201 shales under dried and as-received conditions can be used to calculate the water-occupied or blocked pore spaces (Table 3). For the S_{LG} , the average differences in the SSA of the micropores, non-micropores, and total pores are 3.94, 10.32, and 14.26 $\rm m^2/g$, respectively, and the average differences in the PV are 0.0008, 0.0059, and 0.0067 $\rm cm^3/g$, respectively (Table 3). For the S_{HG} , the average differences in the SSA of micropores, non-micropores, and total pores

are 2.51, 15.73, and 18.23 $\rm m^2/g$, respectively, and the average differences in the PV are 0.0005, 0.0055, and 0.0060 $\rm cm^3/g$, respectively (Table 3).

The water-occupied or blocked pore space is ineffective for shale gas storage. In this study, the effective pore structures of the Z201 shales were quantitatively characterized by the proportion of the effective pore structure to the total pore structure ($P_{\rm E}$) (Gao et al., 2022). The results indicate that pore water in shales can obviously reduce pore space. For the $S_{\rm LG}$, the average water-occupied

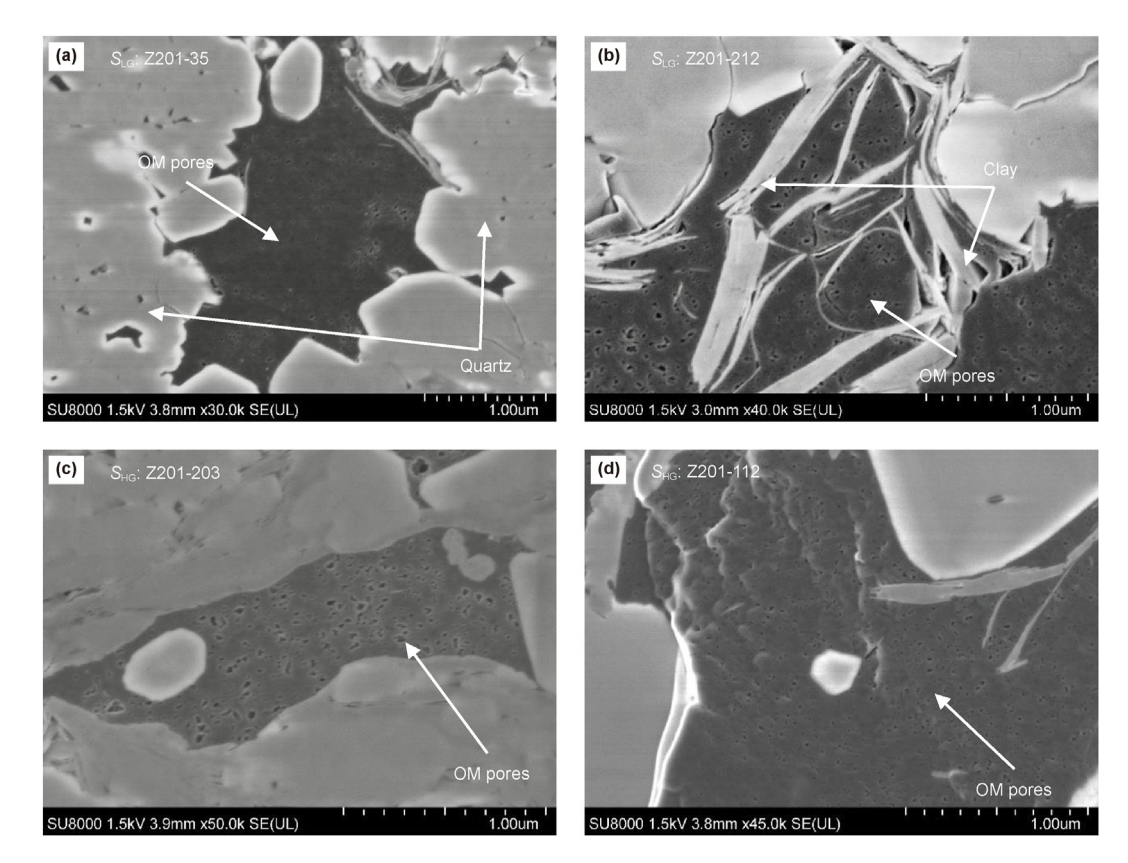


Fig. 5. Typical scanning electron microscope (SEM) images of the deep and ultra-deep Z201 shales. **(a)** Organic matter (OM) pores and brittle-hosted pores of the shales with low gas-in-place contents (S_{LG}); **(b)** OM pores and clay-hosted pores of the S_{LG} ; (**(c)**, **(d)**) OM pores of the shales with high gas-in-place contents (S_{HG}), and inorganic matter (IM) pores barely developed in the S_{HG} .

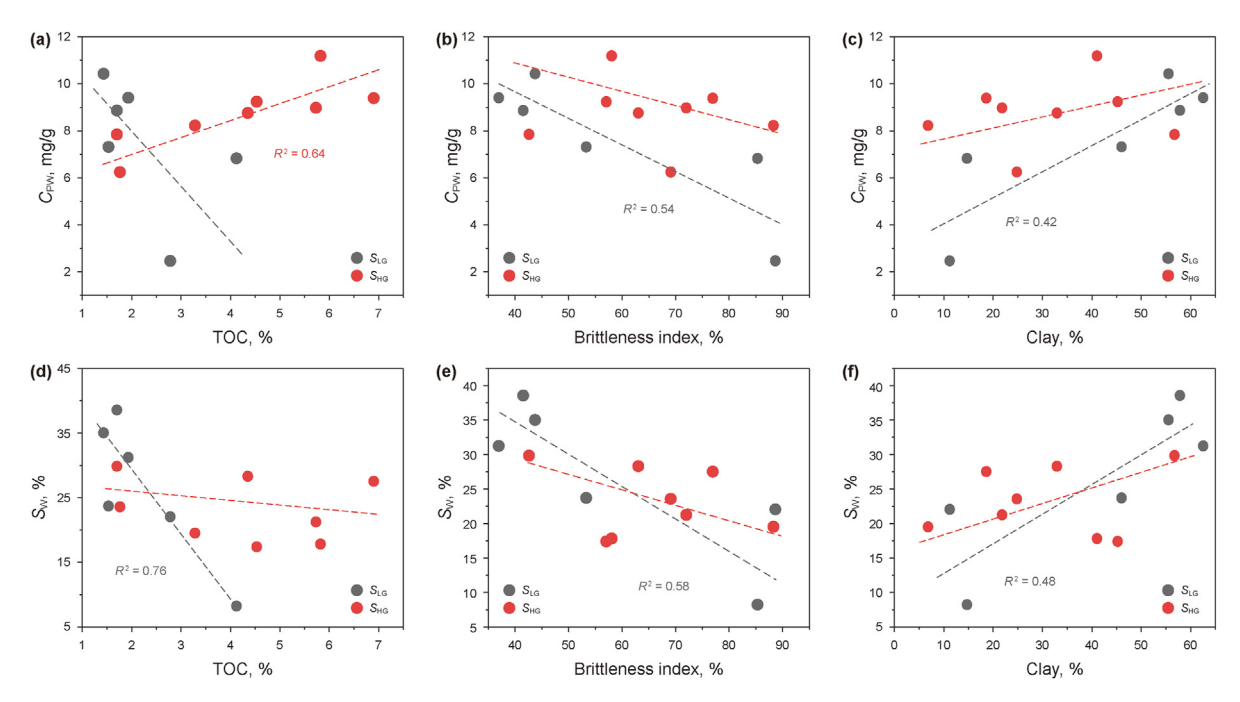


Fig. 6. Correlations between the total organic carbon (TOC) content ((a), (d)), brittleness index ((b), (e)), clay mineral content ((c), (f)), pore water content (C_{PW}) and water saturation (S_W) of the deep and ultra-deep Z201 shales.

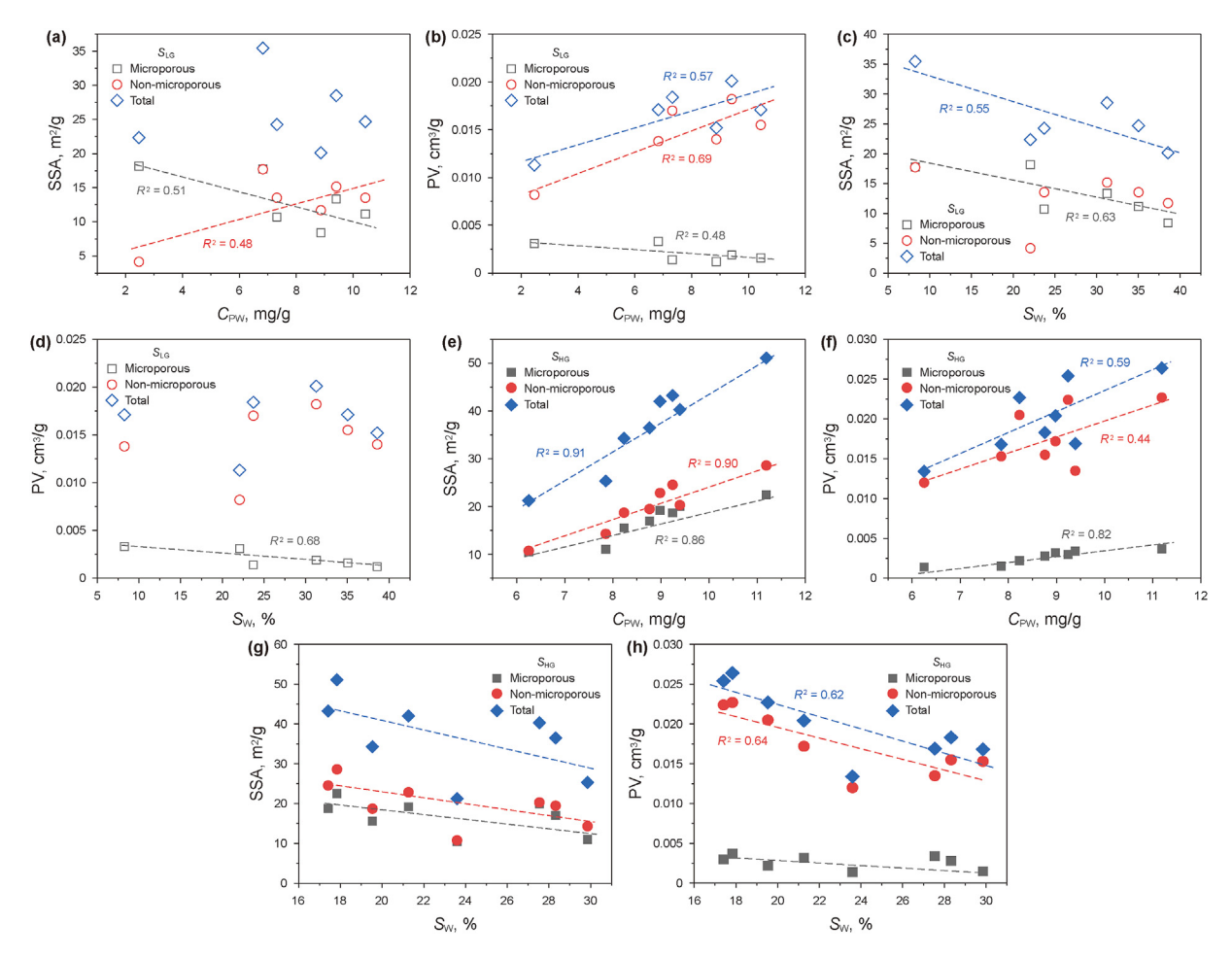


Fig. 7. Correlations between the specific surface area (SSA) and pore volume (PV) with pore water content (C_{PW}) $((\mathbf{a}), (\mathbf{b}), (\mathbf{e}), (\mathbf{f}))$ and water saturation (S_W) $((\mathbf{c}), (\mathbf{d}), (\mathbf{g}), (\mathbf{h}))$ of the deep and ultra-deep Z201 shales.

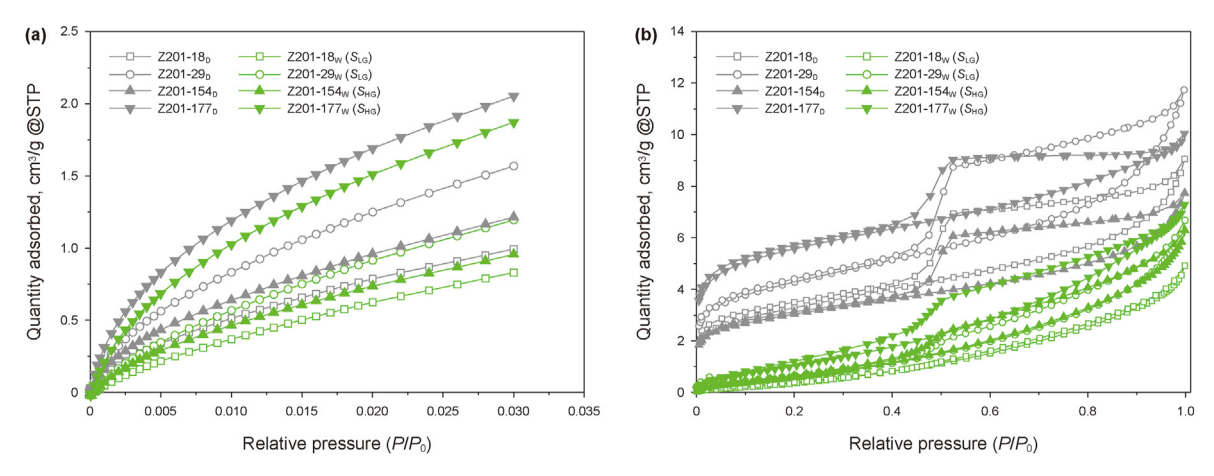


Fig. 8. Typical low-pressure CO₂ adsorption (LPCA) (a) and low-pressure N2 adsorption (LPNA) (b) isotherms of the deep and ultra-deep Z201 shales under dried and as-received conditions.

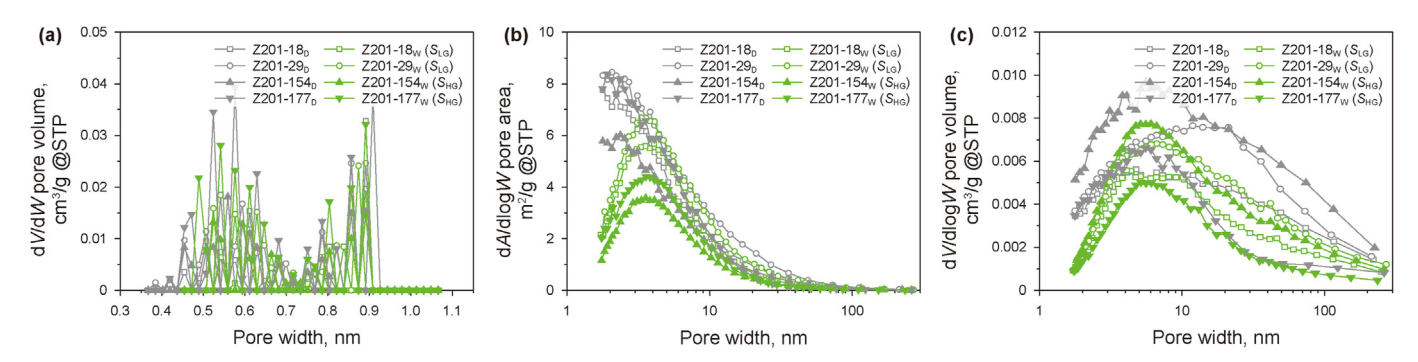


Fig. 9. Typical pore size distributions (PSDs) of micropore volume (PV) (a) and non-micropore specific surface area (SSA) (b) and PV (c) of the deep and ultra-deep Z201 shales under dried and as-received conditions.

Table 3Differences in the pore structure of the deep and ultra-deep Z201 shales under as-received and dried conditions.

Samples	Micropores					icropores			Total pores				
	SSA,	Percentage,	PV,	Percentage,	SSA,	Percentage,	PV,	Percentage,	SSA,	Percentage,	PV,	Percentage,	
	m ² /g	%	cm ³ /g	%	m ² /g	%	cm ³ /g	%	m ² /g	%	cm ³ /g	%	
Z201-18	1.18	14.03	0.0004	33.33	10.04	85.74	0.0064	45.71	11.22	55.77	0.0068	44.74	S_{LG}
Z201-25	1.39	12.47	0.0005	31.25	11.94	88.25	0.0081	52.26	13.33	54.01	0.0086	50.29	
Z201-29	3.03	22.70	0.0007	36.84	12.75	84.10	0.0079	43.41	15.78	55.35	0.0086	42.79	
Z201-35	1.29	12.04	0.0003	21.43	9.99	73.78	0.0043	25.29	11.28	46.52	0.0046	25.00	
Z201-85	1.72	15.59	0.0004	26.67	12.26	85.73	0.0064	41.83	13.98	55.19	0.0068	40.48	S_{HG}
Z201-102	2.85	18.33	0.0004	18.18	13.49	72.02	0.0047	22.93	16.34	47.67	0.0051	22.47	
Z201-108	2.08	11.12	0.0005	16.67	17.16	69.93	0.0053	23.66	19.24	44.49	0.0058	22.83	
Z201-112	2.90	12.89	0.0006	16.22	21.95	76.75	0.0087	38.33	24.85	48.63	0.0093	35.23	
Z201-154	2.28	21.76	0.0004	28.57	8.27	76.93	0.0023	19.17	10.55	49.69	0.0027	20.15	
Z201-177	1.41	8.29	0.0004	14.29	15.42	79.20	0.0042	27.10	16.83	46.15	0.0046	25.14	
Z201-186	2.99	15.58	0.0005	15.63	18.28	80.04	0.0057	33.14	21.27	50.61	0.0062	30.39	
Z201-203	3.84	19.20	0.0005	14.71	18.97	93.45	0.0068	50.37	22.81	56.60	0.0073	43.20	
Z201-210	14.23	78.32	0.0021	67.74	2.27	54.57	0.0038	46.34	16.50	73.89	0.0059	52.21	S_{LG}
Z201-212	2.49	14.03	0.0006	18.18	14.95	84.46	0.0049	35.51	17.44	49.20	0.0055	32.16	

Note: SSA—specific surface area; PV—pore volume.

SSA percentages of micropores, non-micropores, and total pores are 25.60%, 78.48%, and 55.79%, respectively, and the average water-occupied PV percentages of micropores, non-micropores, and total pores are 34.80%, 41.42%, and 41.20%, respectively (Table 4 and Fig. 10). For the *S*_{HG}, the average water-occupied SSA percentages of micropores, non-micropores, and total pores are 15.35%, 79.26%, and 49.88%, respectively, and the average water-occupied PV percentages of micropores, non-micropores, and total pores are

18.87%, 32.07%, and 29.99%, respectively (Table 4 and Fig. 10). The $P_{\rm E}$ is different for pores with different pore widths. The $P_{\rm E}$ values of the micropores SSA and PV are significantly and slightly greater than that of non-micropores SSA and PV, respectively. In addition, the $P_{\rm E}$ values of the micropores SSA are slightly greater than that of micropores PV, while the $P_{\rm E}$ values of non-micropores SSA are obviously less than that of the non-micropores PV (Table 3 and Fig. 10). Overall, the $P_{\rm E}$ values of the $S_{\rm HG}$ are greater than that of the $S_{\rm LG}$,

Table 4 Effective pore structures of the deep and ultra-deep Z201 shales.

Samples	Percentages o	of the effective pore s	tructure, %		Percentages of the water-occupied pore structure, %					
	SSA		PV		SSA		PV			
	Micropores	Non-micropores	Micropores	Non-micropores	Micropores	Non-micropores	Micropores	Non-micropores		
Z201-18	35.93	8.30	5.26	50.00	5.86	49.90	2.63	42.10	S_{LG}	
Z201-25	39.54	6.44	6.43	43.27	5.63	48.38	2.92	47.37		
Z201-29	36.20	8.45	5.97	51.24	10.63	44.72	3.48	39.31		
Z201-35	38.85	14.64	5.98	69.03	5.32	41.20	1.63	23.37		
Z201-85	36.76	8.06	6.55	52.98	6.79	48.40	2.38	38.10	$S_{\rm HG}$	
Z201-102	37.05	15.29	7.93	69.60	8.31	39.35	1.76	20.71		
Z201-108	38.45	17.06	9.84	67.32	4.81	39.68	1.97	20.87		
Z201-112	38.36	13.01	11.74	53.03	5.68	42.96	2.27	32.96		
Z201-154	38.62	11.68	7.46	72.39	10.74	38.95	2.98	17.17		
Z201-177	42.75	11.10	13.11	61.75	3.86	42.28	2.19	22.95		
Z201-186	38.54	10.85	13.23	56.37	7.11	43.50	2.45	27.94		
Z201-203	40.10	3.30	17.16	39.65	9.53	47.07	2.96	40.24		
Z201-210	17.64	8.46	8.85	38.94	63.73	10.17	18.58	33.63	S_{LG}	
Z201-212	43.05	7.76	15.79	52.04	7.02	42.17	3.51	28.66		

Note: SSA—specific surface area; PV—pore volume.

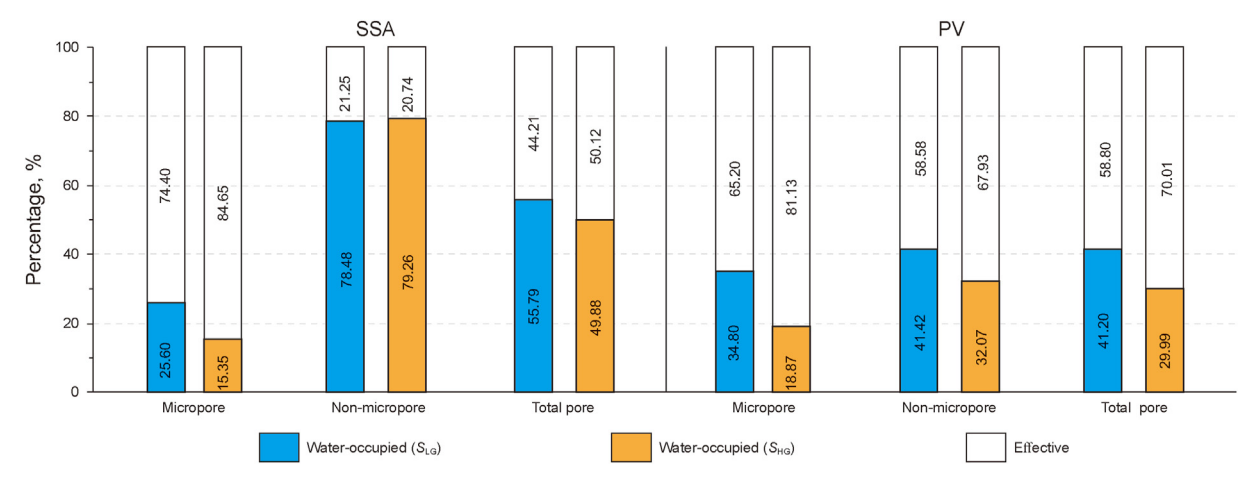


Fig. 10. Percentages of the effective pore specific surface area (SSA) and pore volume (PV) for the deep and ultra-deep Z201 shales.

which is one reason for the high GIP content of the S_{HG}.

Based on the pore development and water-bearing characteristics, an effective pore model of the Z201 shales was preliminarily established in this study (Fig. 11). For the S_{LG} , the SSA P_E values of micropores, non-micropores, and total pores are 35.20%, 9.01%, and 44.21%, respectively, and the PV P_E values of micropores, non-micropores, and total pores are 8.05%, 50.75%, and 58.80%, respectively. For the S_{HG} , the SSA P_E values of micropores, non-micropores, and total pores are 38.83%, 11.29%, and 50.12%, respectively, and the PV P_E values of micropores, non-micropores, and total pores are 10.88%, 59.14%, and 70.02%, respectively. The effective pore structure model indicates that the most of the effective PV and SSA of the Z201 shales are contributed by non-micropores and micropores, respectively. In addition, both the effective SSA and PV of micropores and non-micropores are greater for the S_{HG} than for the S_{LG} (Fig. 11).

Because the water-occupied percentage of the SSA is greater than that of the PV, pore water has a more significantly impact on the SSA than on the PV. This is may be attributed to the majority of the water in shale pores existing in an adsorbed state on the pore surfaces (Li et al., 2021a). In addition, the percentages of water-occupied SSA and PV are greater for non-micropores than for micropores. This phenomenon may be because the non-micropores mainly consist of hydrophilic IM pores, while the micropores

mainly consist of hydrophobic OM pores (Li et al., 2021b). In general, the pore water of deep and ultra-deep Z201 shales is primarily adsorbed in clay-hosted pores with pore widths <10 nm, and the OM micropores contain small amounts of pore water.

4.6. The controlling factors on the GIP content

Because the S_{LG} and the S_{HG} of well Z201 underwent similar diagenetic, thermal, and tectonic evolution processes, the differences in the GIP content between the S_{LG} and the S_{HG} are probably attributed to their OM and IM compositions, pore development and water-bearing characteristics. Based on these characteristics, the main factors controlling the high GIP content in the deep and ultradeep Z201 shales were analyzed in this study.

Compared to the $S_{\rm LG}$ and the Lower Cambrian shales in other areas, the $S_{\rm HG}$ has significantly larger pore spaces. The porosity of the $S_{\rm HG}$ is comparable to that of the Lower Silurian shales with high GIP contents in the Sichuan Basin. The main reasons for the advantageous pore development of the $S_{\rm HG}$ were explained in this study. The OM and IM compositions of shales largely affect their pore development and water-bearing characteristics. The $S_{\rm HG}$ has a high TOC content and brittleness index, which promotes the development and protection of shale pores and reduces the $S_{\rm W}$ of shales. Overall, the $S_{\rm HG}$ have a greater pore structures than the $S_{\rm LG}$.

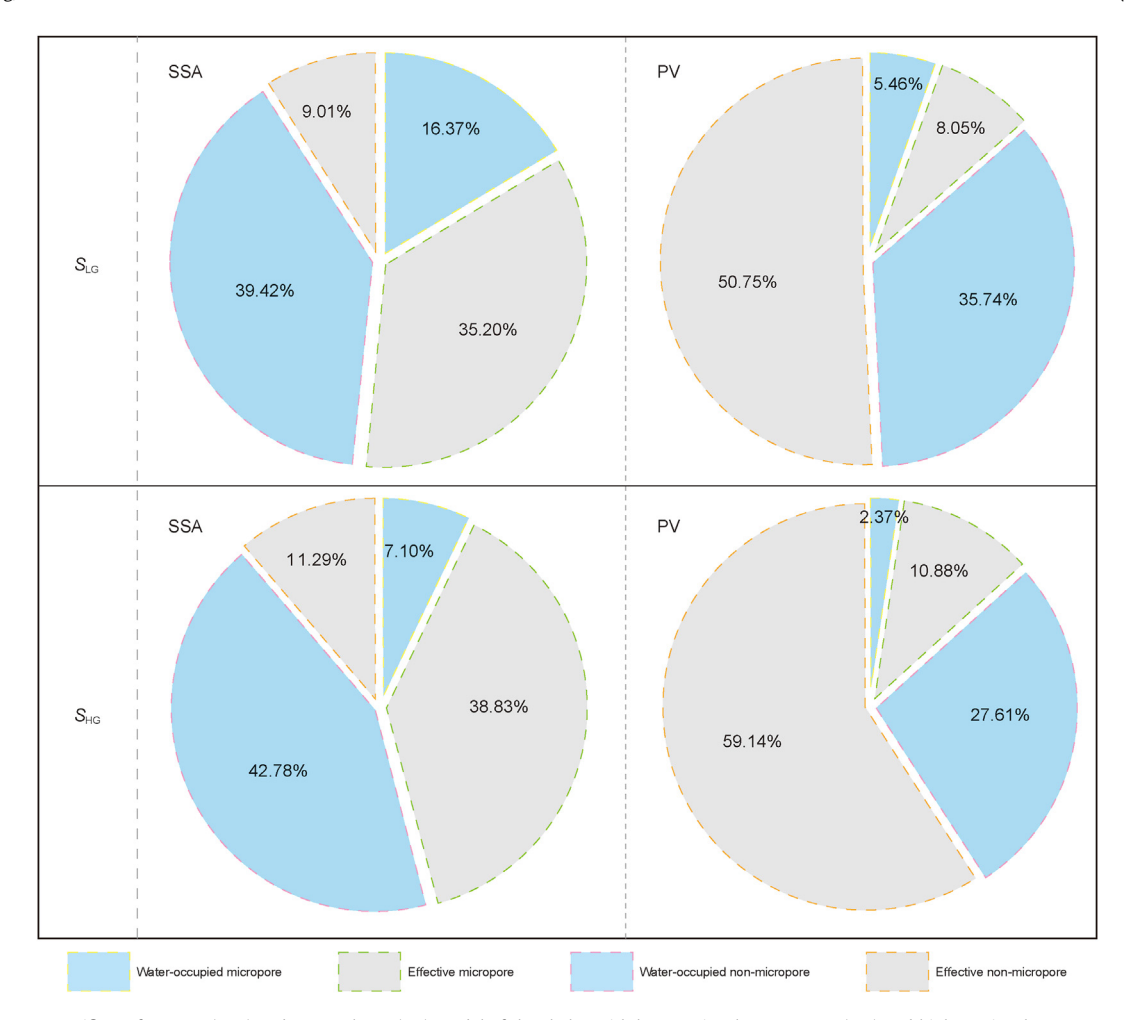


Fig. 11. Effective pore specific surface area (SSA) and pore volume (PV) model of the shales with low gas-in-place contents (S_{LG}) and high gas-in-place contents (S_{HG}) of the well Z201.

For example, the porosity and SSA of the former shales are 69.07% and 41.94% greater than those of the latter shales, respectively. Additionally, the $S_{\rm W}$ of the $S_{\rm HG}$ is smaller than that of the $S_{\rm LG}$, and the presence of pore water further increased the difference in the effective pore space between the $S_{\rm HG}$ and the $S_{\rm LG}$. Actually, the effective porosity of the $S_{\rm HG}$ is approximately 1.7 times greater than that of the $S_{\rm LG}$.

The Lower Cambrian shales in the intracratonic sag were deposited continuously with the underlying Maidiping Formation, and no large-scale folds or faults developed, indicating strong self-sealing properties and effectively reducing the transport and diffusion of shale gas, resulting in the overpressure of the Lower Cambrian shales (Lei et al., 2021; Wang et al., 2021). However, outside the intracratonic sag, the incomplete development of the Lower Cambrian shales and underlying strata led to poor stratigraphic sealing. The weathering crust of the Dengying Formation is a pathway for gas escape, which is unfavorable for the enrichment of the Lower Cambrian shale gas (Liu et al., 2015).

4.7. Favorable exploration areas for deep and ultra-deep Lower Cambrian shale gas

In this study, we propose that great effective pore spaces are the main reason for the high GIP of the deep and ultra-deep Lower Cambrian shales. The great effective pore space of the deep and ultra-deep Lower Cambrian shales requires three basic conditions.

First, organic-rich shales developed in deep-water shelf facies and have high TOC contents and sapropelic kerogen types, which benefited the development of OM pores. Second, the shale strata have low C_{PW} and S_{W} . During the hydrocarbon generation and expulsion processes, most of the water in shale pores is drained by the displacement drainage of liquid hydrocarbons and evaporation drainage of gaseous hydrocarbons (Liu et al., 2015). Third, the pore structures of the shales were well preserved during late tectonic evolution. The overpressure of the shale strata is beneficial for the preservation of shale pores. The pressure coefficient is generally greater than 2.0 in the Z201 shales. Therefore, the Lower Cambrian shales with great effective pore spaces are the most favorable exploration targets for the deep and ultra-deep Lower Cambrian shale gas in the Sichuan Basin.

The breakthrough of the Lower Cambrian shale gas in well Z201 provided important guidance for the subsequent exploration of the deep and ultra-deep shale gas. The deep and ultra-deep Lower Cambrian shales in the Mianyang-Changning intracratonic sag mainly developed in deep-water shelf facies; because these shales with type I and type IIa original kerogen generally have high TOC contents, they have favorable conditions for the development of OM pores. In addition, the low $C_{\rm PW}$ and $S_{\rm W}$ of the Lower Cambrian shales vary in different structural regions. For example, in the Weiyuan anticlinal structure area, the $S_{\rm W}$ of the shale decreases gradually from the anticlinal core region to the two anticlinal wing regions. Therefore, the Lower Cambrian shales located in low

structural regions have low water-bearing extents, which is conducive to the increase of effective pore spaces. Moreover, the sedimentary thickness may affect the development of pores in shales because thick shales generally exhibit a low efficiency of hydrocarbon expulsion, and the cracking of retained hydrocarbons at high maturity easily leads to the formation of high pressure in shale strata, which benefits the preservation of shale pores.

The organic-rich Lower Cambrian shales that developed in the deep-water shelf facies within the Mianyang-Changning intracratonic sag, especially in the Ziyang area around well Z201, have a high sedimentary thickness and benefit pore development and preservation, and they are potential targets for the deep and ultradeep shale gas exploration.

Based on the above considerations, the Lower Cambrian shales in the Ziyang area, located in the center of the Mianyang-Changning intracratonic sag, have a similar depositional environment to that of the Z201 shales and a thickness of more than 300 m, which indicates a great shale gas potential. The Lower Cambrian shales in the Ziyang block cover more than 4800 km². According to the average GIP content (7.2 m³/t) of the Z201 shales, the estimated shale gas resources in the Ziyang block exceed 14×10^{12} m³ (Fig. 1(a)).

5. Conclusions

Based on the shale samples from the first Lower Cambrian highyield gas well Z201, we studied the water-bearing, pore development, and geochemical characteristics of the deep and ultra-deep Lower Cambrian shales, and investigated the differences and primary reasons for high GIP content.

Compared to the S_{LG} , the S_{HG} has high TOC content and porosity, and low water-bearing extent. The average TOC content and maturity of the S_{HG} is 4.26% and 3.70% respectively. The porosity of the S_{HG} is 4.08%–6.16% and dominated by OM pores. The C_{PW} and S_{W} of the S_{HG} is 6.25–11.19 mg/g and 17.41%–29.85%, respectively, and the pore water is primarily stored in clay-hosted pores with pore widths <10 nm.

The effective porosity of the $S_{\rm HG}$ is 4.16%, is 1.7 times greater than that of the $S_{\rm LG}$, which is the main factors controlling the GIP contents of the deep and ultra-deep Lower Cambrian shales. The Lower Cambrian shales in the Ziyang area, have a high TOC content and effective porosity, is benefits for the preservation of shale gas, and they are the most promising targets for the exploration of the Lower Cambrian shale gas.

CRediT authorship contribution statement

Hai-Tao Gao: Writing — review & editing, Writing — original draft, Resources, Methodology, Investigation, Formal analysis, Data curation, Conceptualization. **Peng Cheng:** Writing — review & editing, Supervision, Resources, Project administration, Methodology, Conceptualization. **Wei Wu:** Resources, Project administration, Data curation. **Chao Luo:** Resources, Investigation, Data curation. **Liang Xu:** Resources, Investigation, Data curation. **Teng-Fei Li:** Resources, Methodology, Investigation, Data curation. **Hai-Feng Gai:** Resources, Methodology, Investigation, Formal analysis, Data curation. **Hui Tian:** Writing — review & editing, Supervision, Project administration, Funding acquisition, Conceptualization.

Declaration of competing interest

The authors declare that they have no known competing financial interests or personal relationships that could have appeared to influence the work reported in this paper.

Acknowledgments

This study was supported by the National Natural Science Foundation of China (41925014). This paper is contribution No. IS-3584 from GIGCAS.

Nomenclature

TOC	Total organic matter
GIP	Gas-in-place
OM	Organic matter
IM	Inorganic matter
PSDs	Pore structure distributions
Q1	The Qiongzhusi 1 member
Q2	The Qiongzhusi 2 member
XRD	X-ray diffractometer
$_{Rmc}R_{o}$	Raman maturity
Dh	D peak
Gh	G peak
Φ	Porosity
$ ho_{ m bulk}$	Apparent density
$\rho_{\rm skeletal}$	Skeleton density
LPCA	Low-pressure CO ₂ adsorption
LPNA	Low-pressure N ₂ adsorption
P/P_0	Relative pressure
SSA	Specific surface area
PV	Pore volume
BJH	Barrett–Joyner–Halenda
BET	Brunauer-Emmett-Teller
DFT	Density functional theory
C_{PW}	Pore water content
S_{W}	Water saturation
S_{HG}	The shales with high GIP content
S_{IG}	The shales with low GIP content

References

 $P_{\rm E}$

Anderson, R.L., Ratcliffe, I., Greenwell, H.C., et al., 2019. Clay swelling - a challenge in the oilfield. Earth Sci. Rev. 98 (3–4), 201–216. https://doi.org/10.1016/i.earscirey.2009.11.003.

The proportion of the effective pore structure in the total pore structure

Berend, I., Cases, J.M., Francois, M., et al., 1995. Mechansim of adsorption and desorption of water-vapor by homoionic montmorillonites .2. the Li⁺, Na⁺, K⁺, Rb⁺ and Cs⁺-exchanged forms. Clays Clay Miner. 43 (3), 324–336. https://doi.org/10.1346/ccmn.1995.0430307.

Borjigin, T., Shen, B.J., Yu, L.J., et al., 2017. Mechanisms of shale gas generation and accumulation in the ordovician wufeng-longmaxi formation, Sichuan Basin, SW China. Petrol. Explor. Dev. 44 (1), 69–78. https://doi.org/10.1016/s1876-3804/17/30009-5

Chalmers, G.R.L., Bustin, R.M., 2008. Lower Cretaceous gas shales in northeastern British Columbia, Part I: geological controls on methane sorption capacity. Bull. Can. Petrol. Geol. 56 (1), 1–21. https://doi.org/10.2113/gscpgbull.56.1.1.

Chang, J.Q., Fan, X.D., Jiang, Z.X., et al., 2022. Differential impact of clay minerals and organic matter on pore structure and its fractal characteristics of marine and continental shales in China. Appl. Clay Sci. 216, 106334. https://doi.org/10.1016/j.clay.2021.106334.

Chen, J., Xiao, X., 2013. Mineral composition and brittleness of three sets of Paleozoic organic-rich shales in China South area. J. China Coal Soc. 38, 822–826 (in Chinese).

Chen, L., Jiang, Z., Liu, K., et al., 2017. Application of low-pressure gas adsorption to nanopore structure characterisation of organic-rich lower Cambrian shale in the Upper Yangtze Platform, South China. Aust. J. Earth Sci. 64 (5), 653–665. https://doi.org/10.1080/08120099.2017.1334705.

Cheng, K., Heidari, Z., 2018. A new method for quantifying cation exchange capacity in clay minerals. Appl. Clay Sci. 161, 444–455. https://doi.org/10.1016/ i.clav.2018.05.006.

Cheng, P., Xiao, X.M., Tian, H., et al., 2022. Differences in the distribution and occurrence phases of pore water in various nanopores of marine-terrestrial transitional shales in the Yangquan area of the northeast Qinshui Basin, China. Mar. Petrol. Geol. 137, 105510. https://doi.org/10.1016/j.marpetgeo.2021.105510.

Cheng, P., Xiao, X.M., Tian, H., et al., 2023. Water-bearing characteristics and their effects on the nanopores of overmature coal-measure shales in the Wuxiang area of the Qinshui Basin, north China. Front. Earth Sci. 17 (1), 273–292. https://

doi.org/10.1007/s11707-022-0988-z.

- Cheng, P., Xiao, X.M., Tian, H., et al., 2018. Water content and equilibrium saturation and their influencing factors of the lower paleozoic overmature organic-rich shales in the upper Yangtze region of southern China. Energy Fuel. 32 (11), 11452–11466. https://doi.org/10.1021/acs.energyfuels.8b03011.
- Curtis, J.B., 2002. Fractured shale-gas systems. AAPG Bull. 86 (11), 1921–1938. https://doi.org/10.1306/61eeddbe-173e-11d7-8645000102c1865d.
- Dai, J.X., Ni, Y.Y., Liu, Q.Y., et al., 2021. Sichuan super gas basin in southwest China. Petrol. Explor. Dev. 48 (6), 1251–1259. https://doi.org/10.1016/s1876-3804(21) 60284-7.
- Dong, H.Z., Zhou, D.S., Deng, Z.Y., et al., 2024. Comparative study of the characteristics of lower cambrian marine shale and their gas-bearing controlling factors in the middle and lower Yangtze areas, south China. Minerals 14, 31. https://doi.org/10.1016/j.marpetgeo.2024.107119.
- Feng, Y., Xiao, X.M., Gao, P., et al., 2023a. Restoration of sedimentary environment and geochemical features of deep marine Longmaxi shale and its significance for shale gas: a case study of the Dingshan area in the Sichuan Basin, South China. Mar. Petrol. Geol. 151, 106186. https://doi.org/10.1016/ i.marpetgeo.2023.106186.
- Feng, Y., Xiao, X.M., Wang, E.Z., et al., 2023b. Origins of siliceous minerals and their influences on organic matter enrichment and reservoir physical properties of deep marine shale in the Sichuan Basin, south China. Energy Fuel. 37 (16), 11982–11995. https://doi.org/10.1021/acs.energyfuels.3c01702.
- Gai, H.F., Tian, H., Xiao, X.M., 2018. Late gas generation potential for different types of shale source rocks: implications from pyrolysis experiments. Int. J. Coal Geol. 193, 16–29. https://doi.org/10.1016/j.coal.2018.04.009.
- Gao, H.T., Cheng, P., Wu, W., et al., 2022. Pore water and its influences on the nanopore structures of deep Longmaxi shales in the Luzhou block of the southern Sichuan Basin, China. Energies 15 (11), 4053. https://doi.org/10.3390/ en15114053
- Gao, H.T., Cheng, P., Wu, W., et al., 2023. Effects of pore water on the heterogeneity in nanopore structures of deep marine shales: a multifractal study on asreceived shale samples from the southern Sichuan Basin, China. Energy Fuel. 37 (13), 9032–9046. https://doi.org/10.1021/acs.energyfuels.3c00547.
- Ghanizadeh, A., Clarkson, C.R., Aquino, S., et al., 2015. Petrophysical and geomechanical characteristics of Canadian tight oil and liquid-rich gas reservoirs: I. Pore network and permeability characterization. Fuel 153, 664–681. https://doi.org/10.1016/j.fuel.2015.03.020.
- Han, S.B., Zhang, J.C., Li, Y.X., et al., 2013. Evaluation of lower cambrian shale in northern Guizhou province, south China: implications for shale gas potential. Energy Fuel. 27 (6), 2933–2941. https://doi.org/10.1021/ef400141m.
- Hao, F., Zou, H.Y., Lu, Y.C., 2013. Mechanisms of shale gas storage: implications for shale gas exploration in China. AAPG Bull. 97 (8), 1325–1346. https://doi.org/ 10.1306/02141312091.
- Huo, F.F., Diao, Z.B., Yuan, Y.Y., et al., 2022. Structural characteristic and shale gas exploration potential of the Lower Canbiran in Guizhou and its periphery China. Fresenius Environ. Bull. 31 (4), 4413–4419.
- Jarvie, D.M., Hill, R.J., Ruble, T.E., et al., 2007. Unconventional shale-gas systems: the Mississippian Barnett Shale of north-central Texas as one model for thermogenic shale-gas assessment. AAPG Bull. 91 (4), 475–499. https://doi.org/ 10.1306/12190606068.
- Jia, C.Z., Zheng, M., Zhang, Y.F., 2012. Unconventional hydrocarbon resources in China and the prospect of exploration and development. Petrol. Explor. Dev. 39 (2), 139–146. https://doi.org/10.1016/s1876-3804(12)60026-3.
- Jiang, P., Wu, J., Zhu, Y., et al., 2023. Enrichment conditions and favorable areas for exploration and development of marine shale gas in Sichuan Basin. Acta Pet. Sin. 44, 91–109. https://doi.org/10.7623/syxb202301006 (in Chinese).
- Katsube, T.J., Williamson, M.A., 1994. Effects of diagenesis on shale nano-pore structure and implications for sealing capacity. Clay Miner. 29 (4), 451–461. https://doi.org/10.1180/claymin.1994.029.4.05.
- Kuila, U., Prasad, M., 2013. Specific surface area and pore-size distribution in clays and shales. Geophys. Prospect. 61 (2), 341–362. https://doi.org/10.1111/1365-2478.12028.
- Lei, Q., Xu, Y., Yang, Z.W., et al., 2021. Progress and development directions of stimulation techniques for ultra-deep oil and gas reservoirs. Petrol. Explor. Dev. 48 (1), 221–231. https://doi.org/10.1016/s1876-3804(21)60018-6.
- Li, C.R., Pang, X.Q., Ma, X.H., et al., 2021a. Hydrocarbon generation and expulsion characteristics of the Lower Cambrian Qiongzhusi shale in the Sichuan Basin, Central China: implications for conventional and unconventional natural gas resource potential. J. Pet. Sci. Eng. 204, 108610. https://doi.org/10.1016/ i.petrol.2021.108610.
- Li, G., Gao, P., Xiao, X.M., et al., 2022a. Lower cambrian organic-rich shales in southern China: a review of gas-bearing property, pore structure, and their controlling factors. Geofluids 2022, 9745313. https://doi.org/10.1155/2022/ 9745313.
- Li, G., Li, Z.Q., Li, D., et al., 2022b. Basement fault control on the extensional process of a basin: a case study from the Cambrian-Silurian of the Sichuan Basin, Southwest China. Geol. J. 57 (9), 3648–3667. https://doi.org/10.1002/gj.4492.
- Li, J., Li, X.F., Wu, K.L., et al., 2016. Water sorption and distribution characteristics in clay and shale: effect of surface force. Energy Fuel. 30 (11), 8863–8874. https:// doi.org/10.1021/acs.energyfuels.6b00927.
- Li, J.H., Li, B.B., Gao, Z., 2021b. Water vapor adsorption behavior in shale under different temperatures and pore structures. Nat. Resour. Res. 30 (3), 2789–2805. https://doi.org/10.1007/s11053-021-09846-0.
- Li, J.Z., Tao, X.W., Bai, B., et al., 2021c. Geological conditions, reservoir evolution and

- favorable exploration directions of marine ultra-deep oil and gas in China. Petrol. Explor. Dev. 48 (1), 60–79. https://doi.org/10.1016/s1876-3804(21) 60005-8
- Li, T.F., Tian, H., Xiao, X.M., et al., 2017. Geochemical characterization and methane adsorption capacity of overmature organic-rich Lower Cambrian shales in northeast Guizhou region, southwest China. Mar. Petrol. Geol. 86, 858–873. https://doi.org/10.1016/j.marpetgeo.2017.06.043.
- Li, X., Jiang, Z.X., Song, Y., et al., 2018. Porosity evolution mechanisms of marine shales at over-maturity stage: insight from comparable analysis between lower cambrian and lower silurian inside and at the margin of the Sichuan Basin, south China. Interpretation 6 (3), T739–T757. https://doi.org/10.1190/int-2017-02211
- Li, X., Lu, S.F., Zhao, S.X., et al., 2024. Gas-in-place content and occurrence state of deep shale gas in the Luzhou area, Sichuan Basin, China. Mar. Petrol. Geol. 160, 106662. https://doi.org/10.1016/j.marpetgeo.2023.106662.
- Liu, H., Luo, S.C., Tan, X.C., et al., 2015. Restoration of paleokarst geomorphology of sinian Dengying Formation in Sichuan Basin and its significance, SW China. Petrol. Explor. Dev. 42 (3), 311–322. https://doi.org/10.1016/s1876-3804(15) 30021-5
- Liu, S.G., Deng, B., Jansa, L., et al., 2018. Multi-stage basin development and hydrocarbon accumulations: a review of the Sichuan Basin at eastern margin of the Tibetan plateau. J. Earth Sci. 29 (2), 307–325. https://doi.org/10.1007/s12583-017-0904-8.
- Liu, S.G., Deng, B., Li, Z.W., et al., 2012. Architecture of basin-mountain systems and their influences on gas distribution: a case study from the Sichuan basin, South China.
 J. Asian Earth Sci. 47, 204–215. https://doi.org/10.1016/i.iseaes.2011.10.012.
- Liu, D.H., Xiao, X.M., Tian, H., et al., 2013. Sample maturation calculated using Raman spectroscopic parameters for solid organics: Methodology and geological applications. Chin. Sci. Bull. 58, 1285–1298 (in Chinese). https://doi.org/ 10.1007/s11434-012-5535-y.
- Liu, W.W., Zhang, K., Jiang, Z.X., et al., 2018. Effect of the hydrothermal activity in the Lower Yangtze region on marine shale gas enrichment: a case study of Lower Cambrian and Upper Ordovician-Lower Silurian shales in Jiangye-1 well. Open Geosci. 10 (1), 582–592. https://doi.org/10.1515/geo-2018-0046.
- Liu, Z.Q., Guo, S.B., Lv, R., 2020. Shale-gas play risk of the lower Cambrian on the Yangtze platform, South China. AAPG Bull. 104 (5), 989–1009. https://doi.org/ 10.1306/10031918148.
- Loucks, R.G., Reed, R.M., Ruppel, S.C., et al., 2012. Spectrum of pore types and networks in mudrocks and a descriptive classification for matrix-related mudrock pores. AAPG Bull. 96 (6), 1071–1098. https://doi.org/10.1306/ 08171111061
- Loucks, R.G., Reed, R.M., Ruppel, S.C., et al., 2009. Morphology, genesis, and distribution of nanometer-scale pores in siliceous mudstones of the Mississippi Baenett shale. J. Sediment. Res. 79 (11–12), 848–861. https://doi.org/10.2110/isr.2009.092.
- Lu, Y.Y., Zhou, J.K., Li, H.L., et al., 2020. Different effect mechanisms of supercritical CO₂ on the shale microscopic structure. ACS Omega 5 (35), 22568–22577. https://doi.org/10.1021/acsomega.0c03200.
- Miao, Y.A., Wang, P.F., Li, X., et al., 2023. Shale gas exploration and development potential analysis of lower cambrian niutitang formation and lower silurian Longmaxi Formation in Northwestern Hunan, south China, based on organic matter pore evolution characteristics. J. Mar. Sci. Eng. 11 (10), 1910. https://doi.org/10.3390/jmse11101910.
- Mu, Y., Hu, Z.M., Chang, J., et al., 2021. Effect of water occurrence on shale seepage ability. J. Pet. Sci. Eng. 204, 108725. https://doi.org/10.1016/j.petrol.2021.108725.
- Nie, H.K., Jin, Z.J., Li, P., et al., 2023. Deep shale gas in the Ordovician-Silurian Wufeng-Longmaxi formations of the Sichuan Basin, SW China: insights from reservoir characteristics, preservation conditions and development strategies. J. Asian Earth Sci. 244, 105521. https://doi.org/10.1016/j.jseaes.2022.105521.
- Ross, D.J.K., Bustin, R.M., 2009. The importance of shale composition and pore structure upon gas storage potential of shale gas reservoirs. Mar. Petrol. Geol. 26 (6), 916–927. https://doi.org/10.1016/j.marpetgeo.2008.06.004.
- Rybacki, E., Meier, T., Dresen, G., 2016. What controls the mechanical properties of shale rocks?-Part II: Brittleness. J. Pet. Sci. Eng. 144, 39–58. https://doi.org/10.1016/j.petrol.2016.02.022.
- Sun, C.X., Nie, H.K., Dang, W., et al., 2021. Shale gas exploration and development in China: current status, geological challenges, and future directions. Energy Fuel. 35 (8), 6359–6379. https://doi.org/10.1021/acs.energyfuels.0c04131.
- Tan, J.Q., Horsfield, B., Mahlstedt, N., et al., 2015. Natural gas potential of Neoproterozoic and lower Palaeozoic marine shales in the Upper Yangtze Platform, South China: geological and organic geochemical characterization. Int. Geol. Rev. 57 (3), 305–326. https://doi.org/10.1080/00206814.2015.1004200.
- Tian, H., Pan, L., Xiao, X.M., et al., 2013. A preliminary study on the pore characterization of Lower Silurian black shales in the Chuandong Thrust Fold Belt, southwestern China using low pressure N₂ adsorption and FE-SEM methods. Mar. Petrol. Geol. 48, 8–19. https://doi.org/10.1016/j.marpetgeo.2013.07.008.
- Tian, H., Pan, L., Zhang, T.W., et al., 2015. Pore characterization of organic-rich lower cambrian shales in qiannan depression of Guizhou Province, southwestern China. Mar. Petrol. Geol. 62, 28–43. https://doi.org/10.1016/j.marpetgeo.2015.01.004.
- Ukaomah, C.F., Sun, M.D., Pan, Z.J., et al., 2023. Experimental and molecular investigation of water adsorption controls in marine and lacustrine shale reservoirs. J. Hydrol. 621, 129672. https://doi.org/10.1016/ji.jhydrol.2023.129672.
- Wang, M.M., Hubbard, J., Plesch, A., et al., 2016. Three-dimensional seismic velocity

structure in the Sichuan basin, China. J. Geophys. Res. Solid Earth 121 (2), 1007–1022. https://doi.org/10.1002/2015jb012644.

- Wang, R.Y., Gu, Y., Ding, W.L., et al., 2016. Characteristics and dominant controlling factors of organic-rich marine shales with high thermal maturity: a case study of the Lower Cambrian Niutitang Formation in the Cen'gong block, southern China. J. Nat. Gas Sci. Eng. 33, 81–96. https://doi.org/10.1016/i.ingse.2016.05.009.
- Wang, Y., Qiu, N.S., Xie, X.M., et al., 2021. Maturity and thermal evolution differences between two sets of Lower Palaeozoic shales and its significance for shale gas formation in south-western Sichuan Basin, China. Geol. J. 56 (7), 3698–3719. https://doi.org/10.1002/gi.4121.
- Wang, Y.F., Zhai, G.Y., Liu, G.H., et al., 2021. Geological characteristics of shale gas in different strata of marine facies in south China. J. Earth Sci. 32 (4), 725–741. https://doi.org/10.1007/s12583-020-1104-5.
- Wei, Z.G., Chu, R.S., Chen, L., et al., 2020. The structure of the sedimentary cover and crystalline crust in the Sichuan Basin and its tectonic implications. Geophys. J. Int. 223 (3), 1879–1887. https://doi.org/10.1093/gji/ggaa420.
- Wu, J., Liang, C., Jiang, Z.X., et al., 2019. Shale reservoir characterization and control factors on gas accumulation of the Lower Cambrian Niutitang shale, Sichuan Basin, South China. Geol. J. 54 (3), 1604–1616. https://doi.org/10.1002/gj.3255.
- Wu, W., Cheng, P., Luo, C., et al., 2023. Gas-in-place content of deep shales and its main controlling factors: a case study on the Wufeng-Longmaxi shales in the middle Luzhou block of the southern Sichuan Basin, China. Energy Fuel. 37 (12), 8296–8310. https://doi.org/10.1021/acs.energyfuels.3c01220.
- Xiao, X.M., Wei, Q., Gai, H.F., et al., 2015. Main controlling factors and enrichment area evaluation of shale gas of the Lower Paleozoic marine strata in south China. Pet. Sci. 12 (4), 573–586. https://doi.org/10.1007/s12182-015-0057-2.
- Xie, G.L., Jiao, K., Deng, B., et al., 2023. Pore characteristics and preservation mechanism of over-6000-m ultra-deep shale reservoir in the Sichuan Basin. Front. Earth Sci. 11, 1059869. https://doi.org/10.3389/feart.2023.1059869.
- Yan, J.F., Men, Y.P., Sun, Y.Y., et al., 2016. Geochemical and geological characteristics of the Lower Cambrian shales in the middle-upper Yangtze area of South China and their implication for the shale gas exploration. Mar. Petrol. Geol. 70, 1–13. https://doi.org/10.1016/j.marpetgeo.2015.11.010.
- Yang, X.G., Guo, S.B., 2020. Porosity model and pore evolution of transitional shales:

- an example from the Southern North China Basin. Pet. Sci. 17 (6), 1512–1526. https://doi.org/10.1007/s12182-020-00481-7.
- Yu, H.Y., Wang, Z.L., Rezaee, R., et al., 2018. Porosity estimation in kerogen-bearing shale gas reservoirs. J. Nat. Gas Sci. Eng. 52, 575–581. https://doi.org/10.1016/iingse.2018.02.012
- Zeng, K.C., Jiang, P.X., Lun, Z.M., et al., 2019. Molecular simulation of carbon dioxide and methane adsorption in shale organic nanopores. Energy Fuel. 33 (3), 1785–1796. https://doi.org/10.1021/acs.energyfuels.8b02851.
- Zhang, B., Wen, S.Y., Yang, K., et al., 2023. Diagenetic evolution sequence and pore evolution characteristics: study on marine-continental transitional facies shale in southeastern Sichuan Basin. Minerals 13 (11), 1451. https://doi.org/10.3390/ min13111451.
- Zhang, K., Jia, C.Z., Song, Y., et al., 2020. Analysis of Lower Cambrian shale gas composition, source and accumulation pattern in different tectonic backgrounds: a case study of Weiyuan Block in the Upper Yangtze region and Xiuwu Basin in the Lower Yangtze region. Fuel 263, 115978. https://doi.org/10.1016/i.fuel.2019.115978.
- Zhang, T.W., Ellis, G.S., Ruppel, S.C., et al., 2012. Effect of organic-matter type and thermal maturity on methane adsorption in shale-gas systems. Org. Geochem. 47, 120–131. https://doi.org/10.1016/j.orggeochem.2012.03.012.
- Zhang, Y.Y., He, Z.L., Jiang, S., et al., 2019. Fracture types in the lower Cambrian shale and their effect on shale gas accumulation, Upper Yangtze. Mar. Petrol. Geol. 99, 282–291. https://doi.org/10.1016/j.marpetgeo.2018.10.030.
- Zhang, Y.Y., He, Z.L., Jiang, S., et al., 2018. Factors affecting shale gas accumulation in overmature shales case study from lower cambrian shale in western Sichuan Basin, south China. Energy Fuel. 32 (3), 3003—3012. https://doi.org/10.1021/acs.energyfuels.7b03544.
- Zhou, S.W., Zhang, D.X., 2023. Adsorbed and free gas occurrence characteristics and controlling factors of deep shales in the southern Sichuan Basin, China. Pet. Sci. 20 (3), 1301–1311. https://doi.org/10.1016/j.petsci.2022.12.006.
- Zou, C.N., Hou, L.H., Hu, S.Y., et al., 2014. Prospect of ultra-deep petroleum onshore China. Energy Explor. Exploit. 32 (1), 19–40. https://doi.org/10.1260/0144-5987.32.1.19.
- Zou, C.N., Zhu, R.K., Chen, Z.Q., et al., 2019. Organic-matter-rich shales of China. Earth Sci. Rev. 189, 51–78. https://doi.org/10.1016/j.earscirev.2018.12.002.